Signal Absorption-Based Range Estimator for Undersea Swarms

by

Commander Brendan O'Neill, USN

B.A., University of Florida (2003)

Submitted to the Joint Program in Applied Ocean Science & Engineering
in partial fulfillment of the requirements for the degree of

Master of Science, Mechanical Engineering

at the

MASSACHUSETTS INSTITUTE OF TECHNOLOGY

and the

WOODS HOLE OCEANOGRAPHIC INSTITUTION

September 2020

Author . . . .
Joint Program in Applied Ocean Science & Engineering
Massachusetts Institute of Technology
& Woods Hole Oceanographic Institution
August 07, 2020

Certified by . . . .
Erin Fischell
Assistant Scientist
Woods Hole Oceanographic Institution
Thesis Supervisor

Certified by . . . .
John Leonard
Samuel C. Collins Professor of Mechanical and Ocean Engineering
Massachusetts Institute of Technology
Thesis Supervisor

Accepted by . . . .
Nicolas Hadjiconstantinou
Chairman, Committee for Graduate Students
Massachusetts Institute of Technology

Accepted by . . . .
David Ralston
Chairman, Joint Committee for Applied Ocean Science & Engineering
Woods Hole Oceanographic Institution

Signal Absorption-Based Range Estimator for Undersea Swarms

by

Commander Brendan O'Neill, USN

Abstract

Robotic swarms are becoming increasingly complex on the surface and in air due to high-speed and reliable communication links, Global Positioning Satellites (GPS), and visual support to relative navigation. However, the limited propagation of these signals in the ocean has impacted similar advances in undersea robotics. Autonomous underwater vehicles (AUVs) often rely on acoustics to inform navigation solutions; however, this approach presents challenges for scalable robotic swarms. Acoustic navigation is a means to inform range and bearing to a target. Many methods for range and bearing estimation, including current low-cost solutions, rely on precision time synchronization or two-way communication to compute ranges as part of a full navigation solution. The high cost of reliable Chip-scale atomic clocks (CSACs) and acoustic modems relative to other vehicle components limits large-scale swarms due to the associated cost-per-vehicle and communications infrastructure. We propose a single, high-cost vehicle with a reliable navigation solution as a "leader" for a scalable swarm of lower-cost vehicles that receive acoustic signals from a source onboard the lead vehicle using a single hydrophone. These lower-cost "followers" navigate relative to the leader according to the preferred behavioral pattern, but for simplicity, we will refer to a simple following behavior in this work. This thesis outlines a method to obtain range estimates to sound sources in which the signal content, including frequency and power at its origin, can be reasonably approximated. Total transmission loss is calculated based on empirical equations for the absorption of sound in seawater and combined with geometric spreading loss from environmental models to estimate range to a source based on the loss at differential frequencies. We refer to this calculation as the signal absorption-based range estimator (SABRE). This method for obtaining range combines with Doppler-shift methods for target bearing based on the maximum frequency detected within a banded limit around a known source frequency. A primary objective for SABRE is to address techniques that support low-cost options for undersea swarming. This thesis's contributions include a novel method for range estimation onboard underwater autonomous vehicles that supports navigation relative to a known source when combined with Doppler-shift methods for target bearing. This thesis seeks to develop the theory, algorithms, and analytical tools required and apply those tools to real-world data sets to investigate the feasibility, sources of error, and accuracy of this new approach to range estimation for underwater swarms.

Thesis Supervisor: Erin Fischell
Title: Assistant Scientist

Woods Hole Oceanographic Institution

Thesis Supervisor: John Leonard
Title: Samuel C. Collins Professor of Mechanical and Ocean Engineering
Massachusetts Institute of Technology

Acknowledgments

I express my eternal gratitude to Professor John Leonard, my research advisor. Without his constant support, I would not have had the opportunities I have enjoyed the past two years. His faith in me, despite my long-term separation from academics, has fundamentally changed my life's trajectory. Professor Leonard continues to educate and mentor me at every turn in my adventures in graduate study. It has been a privilege to interact with such an incredible mind in the field of autonomous robotics, and his guidance has set a high standard for future work. Dr. Leonard fueled my professional development by allowing me to represent our group at the 2018 MIT-Portugal Annual Conference. He consistently engaged in my research efforts and facilitated opportunities to assist with Synchronized Position Hold Engage and Reorient Experimental Satellite (SPHERES) experiments onboard the International Space Station. These experiences have been truly enlightening and have reinforced my passion for autonomous robotics in undersea and space environments.

During the summer of 2019, Professor Leonard encouraged me to work with Dr. Erin Fischell, who later became my co-advisor. Dr. Fischell immediately fast-tracked my research efforts through direct engagement in autonomous underwater vehicles and real-world field experiments. Dr. Fischell's ability to drive the research goals of her entire group and many collaborators, maintain complete visibility on academic performance, and create a welcoming environment in which researchers could thrive consistently impressed me. Dr. Fischell was critical in the day-to-day goals of my research and provided sound guidance on how to solve theoretical problems and troubleshoot hardware for data collection. After sixteen years as a Naval Officer, I never expected to learn as much about leadership and management as I did in my work with Dr. Fischell.

6

clear evidence that to make a difference, one needs only to set their minds to the task and never quit.

Thanks to my lab colleagues in the Marine Unmanned Robotics and Acoustics Lab at WHOI and the Marine Robotics Group at MIT for their support, late-night discussions, and continual willingness to "go to the whiteboard and figure it out." These groups are evidence that it truly takes a village.

During my graduate studies, I have come to understand new and different kinds of stress, which I have ultimately enjoyed thoroughly. However, without the outlet I found in the MIT Wrestling Club, I sincerely doubt I would have found the balance I eventually did during my first two years. Wrestling is a sport that instills the resilience required to work your way up when knocked down and the knowledge that rewards come through perseverance and effort. These skills have proven invaluable well beyond the wrestling room. Thanks to my fellow wrestlers and the MIT Wrestling Coaches for the privilege of training with you.

To my wife, dogs, family, and friends; Thank you for your understanding. Thank you for the canceled vacations, the lack of communication, and the need for constant focus to meet these challenges. Thank you in advance for continuing to understand. No matter what level of understanding I can attain concerning autonomous robotic navigation, I know that I would lose my way without your support.

Contents

List of Figures

List of Tables

Chapter 1

Introduction

This chapter provides the motivation that led to this thesis, and a brief overview for each chapter.

1.1   Motivation

Robotic swarms are executing tasks that require diverse platforms and are dependent on careful coordination in space and time. These tasks range from entertainment, environmental sampling, map generation, and even time-sensitive search and rescue operations. Swarms are significantly more difficult in ocean environments due to the rapid attenuation of high-frequency signals in an underwater environment. However, robotic swarms have immense potential to expand existing capabilities in an environment that varies widely across latitude, longitude, depth, and time. Billions of dollars have been spent on cabled ocean observatories to address the difficulties in collecting long-time realizations across comparable spatial areas of focus [1], but this approach has limits due to its high cost, lack of mobility, and limited reach. For these reasons, the prospect of a scalable method for undersea robotic swarms can increase awareness of how phenomena in an ocean environment vary across these multiple dimensions. Current swarming techniques for undersea operations have limits in scalability due to cost-per-vehicle and communication techniques that do not support large numbers of robots. Addressing the limits on underwater robotic swarming will drastically increase accessibility to the advantages of a multi-agent approach. Increased accessibility to undersea robotic swarms will enhance prediction models for weather events, algae blooms, and climate change monitoring. Swarms of underwater vehicles can sample large volumes in space while

taking simultaneous measurements in time that expand input for predictive models and allow complex vehicle formations to support operational requirements. Air and ground-based robotics can rely on sensors that utilize vision and radio communication in order to calculate and share full navigation solutions in real-time [2] [3] [4] [5]. However, while complex even above water, these techniques have severe limitations in an undersea environment due to the rapid attenuation of most in-air communication signals.

Underwater communication is generally addressed through lower-frequency acoustic signals, pre-positioned beacons, precision clocks, and intermittent surfacing to update position fixes. These approaches have significant barriers when it comes to large-scale swarms. Current methods for underwater navigation, particularly swarming, rely on a combination of Inertial Mapping Units, precision time synchronization for acoustic signals, and cooperative localization techniques. Such methods necessitate precision timing between the source and receiver or the ability to transmit detailed localization information between platforms, both of which can limit scalability due to cost and communication architecture. In addition, many current methods cannot achieve localization passively, and require active signals in the environment which may be undesirable. Thus, otherwise low-cost autonomous underwater vehicles (AUVs), must rely on a combination of costly chip-scale atomic clocks (CSAC) and acoustic modems for reliable localization which can account for half the cost of a $10k underwater vehicle. The motivation for this thesis is to address these high-cost items as obstacles to scalable AUV swarms.

1.2   Thesis Overview

This thesis evaluates the feasibility and effectiveness of range estimations via differential frequency attenuation in seawater. Signals are evaluated through various processing techniques to calculate the received pressure level at a single hydrophone at two adequately separated frequencies. This method relies on known source frequency content to calculate the difference in total transmission loss at each frequency. Differential frequency transmission loss and environmental modelling provide the basis for range estimation within a bounded error.

Chapter 2 reviews background and related works such as the acoustic methods for long baseline (LBL), short baseline (SBL), and ultra-short baseline (USBL) localization. A short discussion on inertial navigation systems (INS) and Doppler velocity logs (DVL) will provide

a baseline for some common sensor payloads. The chapter includes a review of acoustic modems for data packet transmission in conjunction with and separate from these systems. A notable difference is that the range estimates from these techniques rely on one-way or two-way travel time (OWTT or TWTT) of acoustic transmissions. There are advantages and associated limitations to these approaches that more clearly enumerate the motivation behind this work.

The theoretical foundations, methods, environmental models, and empirical equations used to estimate range through measured transmission loss form Chapter 3. This chapter will review the signal processing techniques necessary for SABRE to analyze real-world hydrophone data. The calculations will give expectations for the performance of differential frequency transmission loss as a means to estimate range. This portion will model several different environments and establish hypotheses for the ideal conditions under which SABRE will succeed. The sources of error and their sensitivity will also be assessed.

Chapter 4 describes the experimental protocols and real-world data collection setup, equipment, and techniques. Due to this thesis's timing, environment options for data collection were severely limited and subject to areas that remained open and safe for collection during the COVID-19 pandemic. While this period was limiting, it provided opportunities to address more difficult collection environments and overcome the many hardware and software challenges presented by single-person experiments. Ultimately, these challenges contributed to a more well-rounded thesis and educational experience. The theory put forth in Chapter 3 provides a basis to evaluate signal detections, estimate ranges, and establish the error bounds for this method based on real-world data collection and ground truth ranges. These results will allow further evaluation of the feasibility and scalability of this methodology.

Chapter 5 contains details on the results and conclusions for the experimental data. This chapter describes the updated experimental protocols and lessons learned. To effectively evaluate this method's potential, Chapter 5 will also compare the algorithm's performance to the current state of the art approaches concerning cost, environmental requirements, and associated error. While we anticipate increased error margins, that error will be bounded over time and mitigated during the mission planning phase with proper vehicle spacing. The cost comparison and error associated with this technique will determine whether it provides a more cost-effective solution for scalable swarm formations in undersea sampling

operations. Chapter 5 will close with an assessment of opportunities for future work along this research path.

Chapter 2

Background

This chapter will provide background on current approaches to localization for AUVs as well as their associated strengths and limitations in large-scale swarm operations.

2.1   Current Methods

Underwater navigation has traditionally addressed the challenges of the rapid attenuation of signals used in surface and air sensing and communication by relying primarily on acoustic signals capable of traveling long distances through the ocean. However, this presents new challenges based on how acoustic signals propagate in an underwater environment. Some obstacles to acoustic sensing and communication include slower update rates due to the speed of sound in water and distinguishing acoustic signals from ambient noise and environmental effects. The fact that many commercial, scientific, and government projects in underwater environments require time scales of weeks and spatial coverage on the order of cubic kilometers further compounds these obstacles [6] [4].

Most non-acoustic sensing methods for undersea navigation utilize inertial navigation systems (INS) to monitor the orientation, velocity, and acceleration of vehicles. These systems approximate the distance and direction traveled over time, a process commonly referred to as dead-reckoning. Modern dead-reckoning systems can provide low-error navigation solutions, but their accompanying error, however small, grows unbounded with time and distance traveled. The error associated with these systems can be minimized through high-cost inertial sensors but is not eliminated and will not scale to long-time measurements or long-distance transits. These systems require a means to reset the error accumulating

from the INS to maintain accurate navigation solutions. Therefore, most underwater navigation techniques utilize INS in conjunction with information from other sensors (aided INS) to maintain a solution within a bounded error [7].

A common sensor pairing for INS is a Doppler velocity log (DVL). DVL's provide 3-axis velocity measurements for marine vehicles to combine with INS data, usually integrated into a Kalman or extended Kalman filter (EKF). The vehicle calculates velocity based on a set of transducers that send acoustic signals to the seabed, and the Doppler shift for the returned signal. While these systems have made significant advances in improved accuracy they do not achieve a bounded error without some reset such as GPS. Also, there can be scenarios that heavily impact the accuracy of an INS/DVL combination such as failed transducers, sudden changes in range to the seabed due to bathymetry, or sudden changes in vehicle depth. Such systems are also less useful in the mid-water column of the deep ocean due to the inability to bottom-track [52] [31] [32].

Amongst these techniques is long baseline localization (LBL), which relies on a set of transponders with known positions to triangulate positions for underwater vehicles. An AUV can then localize via the time of flight (TOF) of acoustic signals from the set of transponders and their arrival at a receiver, typically onboard the AUV. However, vehicles must also be able to identify from which transponder each signal originated. Vehicles can establish this criterion based on known signal content from each transponder, the geometric structure of the receiver, or using an acoustic modem, discussed later in this section. The requirements for a prepositioned range of beacons with known locations can incur a high cost. This increase in cost is often tied to the need for a support platform of some kind, such as a surface, underwater, or airborne vessel to assist with transponder localization and recovery. This method also limits the spatial reach for effective navigation solutions to the range of the pre-deployed transponders. Setup, maintenance, and environmental factors can present logistical challenges for LBL systems due to the costs of delays that could extend timelines for support and recovery. LBL systems require a detailed sound speed profile for the area of operations to localize AUVs accurately, and most utlize two-way communication for navigation solutions. This two-way communication places a limit on the number of platforms due to the communications architecture. However, if the setup and high-cost are feasible, LBL solutions offer highly reliable calculations for undersea localization [8].

Short baseline (SBL) techniques closely resemble LBL, but typically utilize a surface

platform to overcome environmental limitations such as ice or insufficient transponder range to support the scope of operations. While this can present a mobile reference platform's advantage, it still uses a similar triangulation method. Typically these systems can only support a fraction of the baseline of an LBL network due to limitations in platform size. The size of the surface platform utilized to support this localization method imposes a limit on the baseline between receivers and the system's accuracy. The use of a mobile platform in the ocean can be costly, and that cost typically rises along with platform size due to increased personnel and fuel requirements. The addition of a mobile surface platform, if it requires persistent human operators, limits the scope of autonomous operations.

Ultra-short baseline (USBL) techniques provide a more compact means to assess distance and bearing between source and receiver. A platform with regular position updates, such as onboard a surface vessel with global positioning satellite (GPS) systems, transmits an interrogation signal to a transponder at the ocean floor or onboard an AUV. This interrogation signal triggers a response from the transponder. The vessel maintains a precisely spaced array of transceiver elements to assess the TOF and phase arrival of incoming signals. USBL techniques assess the angle between the source and receiver through the differences in phase arrival at each element on the transceiver array. The TOF of the signal facilitates a range estimation based on the local sound speed profile. Inverse USBL (iUSBL) utilizes the same technique in reverse with transceiver elements onboard an AUV and signals originating from a platform with a known position, but the principle remains the same. iUSBL has the advantage that an AUV can self-localize via one-way communication and onboard processing relative to the platform with a known position. This condition makes iUSBL a more scalable solution based on the communications architecture. [9] [10]

LBL, SBL, and USBL systems that integrate acoustic modems can communicate more detailed localization data between platforms via transmitted data packages and the assessed TOF of signals. These data package exchanges allow platforms with a known position to explicitly share localization data, which improves the overall localization solution. For example, rather than limiting the assessed position to TOF and angle estimates, a USBL system could include GPS information transmitted via a surface platform's acoustic modem to reduce the error in its localization. Also, AUVs with acoustic modems can perform cooperative localization between vehicles by sharing their assessed positions in these data packages. If at least one vehicle is capable of a reliable navigation solution, this removes the

23

necessity for fixed beacons or a surface platform. AUV swarms can use acoustic modems to maintain reliable navigation solutions via periodic surfacing for GPS fixes or feature-based navigation methods such as simultaneous localization and mapping (SLAM). An AUV that surfaces or observes an underwater feature that aids localization can then share that data with other vehicles via an acoustic modem. In [11], direct measurements between vehicles are combined with measurements to other features in the operational area to inform a more reliable solution. However, these options are restrictive in their scalability based on the sensors required for reliable navigation without outside support and detailed communication between multiple platforms. The environment must also have detectable features in order for this approach to enhance localization. In many operational scenarios, there is no opportunity to surface for a GPS fix, such as operations under the ice. Acoustic modems also present limitations on scalability for swarms due to the number of vehicles communicating and the bandwidth required to pass the necessary detail in an underwater-swarming scenario. Time-division multiple-access (TDMA) protocols that allow multiple platforms to communicate are the primary limiting factor regarding scalability. This approach can enhance the reliability of each vehicle's navigation but limits the number of total vehicles that can reliably share the communication architecture. The high potential for data loss in underwater communication environments makes sharing detailed location information to a large number of vehicles through acoustic modems both challenging and high-risk. Additional sensors, such as side-scan sonar or powerful cameras, are required to gather and disseminate feature-based navigation details for cooperative localization [12] [11]. Acoustic modems bring compelling advantages to underwater localization and incur challenges that become more problematic in large-scale robotic swarms.

The techniques listed thus far require specialized equipment to maintain error bound localization estimates. Most architectures require close time synchronization between vehicles to obtain range and bearing solutions based on the TOF of acoustic signals. Other approaches address this challenge through two-way communication and estimate range based on the round-trip TOF for an initial transmission and reply. Range and bearing estimates based on one-way travel time (OWTT) of acoustic signals necessitate precision timing between the source and receiver and require devices such as chip-scale atomic clocks (CSACs). CSACs are currently the standard for low-cost AUVs but account for about half the baseline vehicle cost and thus profoundly impact cost at scale. This assessment is based on a low-

cost underwater vehicle being in the $10k range and the CSAC accounting for up to $5,500 of that amount. These cost estimates rely on previous work by Fischell et al. in [14] and common low-cost underwater vehicles such as described in [28] and [29]. Two-way travel time (TWTT) systems reduce the need for closely synchronized clocks but require vehicles that can receive and respond to incoming signals, usually via an acoustic modem [13].

2.2 Doppler Shift for Bearing Estimates

This thesis proposes a different method for range and bearing-based acoustic navigation relative to a beacon, and with bounded error through information gathered from a single hydrophone onboard a very-low-cost AUV. By relaxing the need for close time synchronization, beamforming, and two-way communication methods the objective is to find the minimum information requirements to localize the AUV in space, driving down the cost and power consumption by orders of magnitude at the expense of precision. The extent of this tradeoff with respect to range is the subject of this thesis.

Since our approach relies on Doppler shift to estimate bearing, this section briefly describes the bearing estimation though the contribution to the overall technique from SABRE is specific to range estimation.

When a sound source and receiver are in relative motion, there is a detectable shift in the frequency recorded at the receiver, known as the Doppler Effect. For the combined leader-follower algorithm to be successful, it must address the relative motion between the receiver onboard the follower AUV in the swarm, and the source onboard the leader. Each follower must estimate the received frequency, f_r, within a band around a known frequency broadcast by the source onboard the leader.

Figure 2-1 shows a two-dimensional example of this approach. The follower AUV's velocity is denoted as v_r in keeping with our receiver notation, and v_s represents the lead vehicle's velocity. $\hat{n}$ represents the vector connecting the follower to the leader. The relative angle between their respective velocity vectors, θ_{rel}, gives strong intuition on the bearing estimate. If our follower AUV has a velocity vector directly in line with the leader then $\theta_{rel} = 0$.

$$f_r = \frac{f_s(c + \vec{v_r} \cdot \hat{n})}{c + \vec{v_s} \cdot \hat{n}} = \frac{f_s(c + |\vec{v_r}|cos(\theta_{rel})}{c + \vec{v_s} \cdot \hat{n}}. \tag{2.1}$$
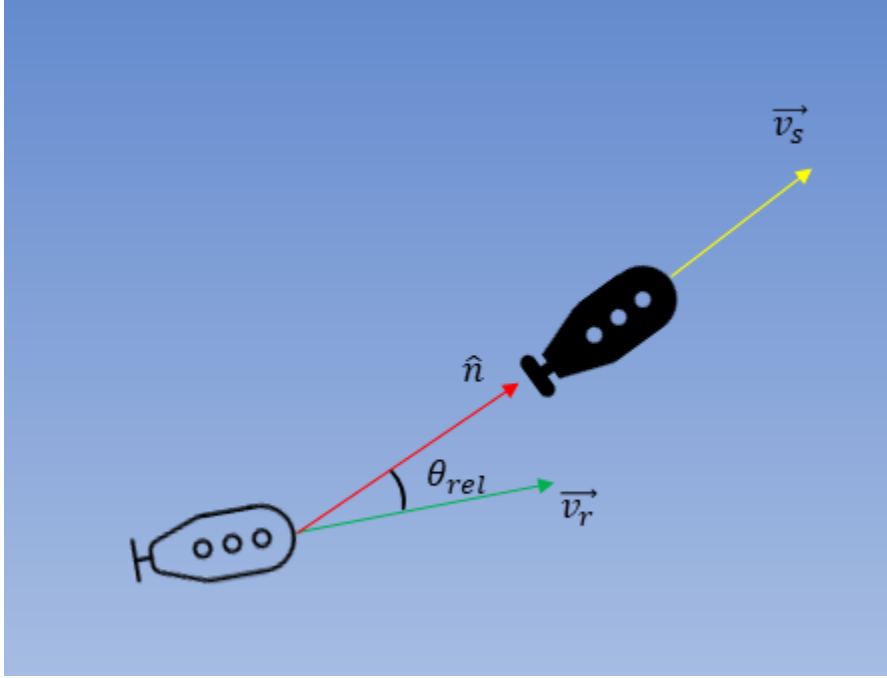
Figure 2-1: Visualization of relative velocities and angles associated with Doppler effect

Equation 2.1 reinforces this intuition as $\theta_{rel} = 0$ produces a maximum in f_r. This outcome is as expected since the Doppler shift increases the frequency observed when the receiver moves toward the source, or at least minimizes the decrease in frequency by minimizing the source's movement away. The follower's velocity, v_r, is subject to feedback control based on the estimated range from the leader, but a continued estimation for the heading is also necessary. The heading estimation is based on the maximum received frequency, assuming that the relative velocity for the leader is unknown, and the follower will continue to adjust heading at the prescribed interval in order to maximize the received frequency within a predetermined band around the source frequency. The follower vehicle thus adjusts heading at a predetermined interval and magnitude to observe Δf_r, where Δf_r is the change in the received frequency due to the heading adjustment.

$$\Delta f_r = f_{r1} - f_{r2} \tag{2.2}$$

If Δf_r is positive, the follower will continue to adjust heading, i.e., turn the same direction. If Δf_r is negative, then the follower will alter its turn in the opposite direction. The interval at which a follower alters course can also be adjusted according to the mission profile to maximize efficiency while allowing for periodic checks on frequency shift. Such

an interval could also be dependent on a predetermined change in the range estimation. Fischell, et al. describe this feedback control method in detail in [14] and the estimate for target bearing provides half the required information for localization. SABRE provides the second half with an estimate for range to accompany bearing to target. To estimate range with a single hydrophone without close time synchronization we explored an environmental property that effects every acoustic measurement in the ocean.

2.3   Absorption of Sound as a Navigational Aid

Most previous studies treat the absorption of sound in seawater based on frequency as a source of distortion. In that context, an acoustics communication system must be robust to the effects of absorption on signal transmission [15] [16]. However, Young proposes the use of a single hydrophone to self-localize an autonomous vehicle, and presents some similarities to our approach [17]. This work focuses on pairing Doppler shift with the waveguide invariant to self-localize via sources of opportunity (SOOs) such as shipping traffic. The waveguide invariant, β, is a parameter that describes the acoustic intensity pattern versus frequency and range. This parameter is specifically related to the slope of the interference patterns represented in this relationship such that for $I(r,f)$ the striations of the interference pattern for a broadband signal have a slope $\frac{\delta f}{\delta r} = \beta(f/r)$. As a single-vehicle application, this method supplements the onboard INS with a bounded error but requires the presence of SOOs to estimate a bearing and range from their position. This method also proposes acoustic updates of automatic identification system (AIS) data and assumes that surface vessels can support acoustic transmitters for their AIS data. This approach also requires the AUV to have equipment that reliably receives the location data, probably via an acoustic modem. The required modems and computational cost associated with this method enable localization; however, they do not provide a scalable solution for low-cost swarming of AUVs. Therefore there is a need for a method that maintains low cost at scale for a swarm of underwater vehicles to maintain formation while transiting a desired area of operations.

This thesis proposes an alternative to the CSACs currently utilized in low-cost AUVs while allowing for range estimation scalable for AUV swarms. In conjunction with Doppler-shift methods to obtain bearing information, range can be estimated with bounded error over time through the differential transmission loss of multi-frequency acoustic signals in seawater.

Our method allows for underwater swarms at set ranges with a single "lead" vehicle equipped with robust navigation and a transceiver. Based on a review of existing methods, this thesis proposes that reliable navigation for a single vehicle may be feasible without significantly impacting the cost-per-vehicle at scale. The contributions proposed in this thesis will be to explore low-cost solutions for underwater vehicle swarms and enhanced options for the spatial and temporal sampling of ocean environments. Increased spatial sampling will support greater efficiency in search operations, allow for more robust environmental modeling, and expand our understanding of undersea processes.

Chapter 3

Methods

As SABRE relies on the absorption of sound in seawater, this chapter reviews impacts from specific chemical compounds in the water column and the methods employed to estimate absorption loss over range from these compounds at specific frequencies. This chapter will include the necessary empirical equations, and derivations for the acoustic properties at the source and receiver.

3.1 Sound Absorption in Seawater

The Francois-Garrison equations form the basis for this section. These equations are derived from theoretical principles, and then adjusted to fit empirical data [18] [19]. The general equation described in the literature combines the effects of pure water, magnesium sulfate, and boric acid in one equation to compute an absorption estimate. While other empirical equations exist, the Francois-Garrison equations are the basis for this work due to their accuracy and inclusion of critical environmental parameters such as pH, temperature, salinity, and depth. Table 3.1 shows the three frequency regions in which each absorption factor dominates. While other chemical reactions impact the absorption of sound in seawater, these phenomena are considered negligible.

A fourth impact region at frequencies lower than 100 Hz is associated with leakage out of the deep sound channel [20]. This work focuses on frequencies higher than one kHz and therefore does not address this very-low-frequency region. Figure 3-1 shows absorption coefficients for seawater and pure water versus frequency. Figure 3-2 shows how these curves vary with temperature.
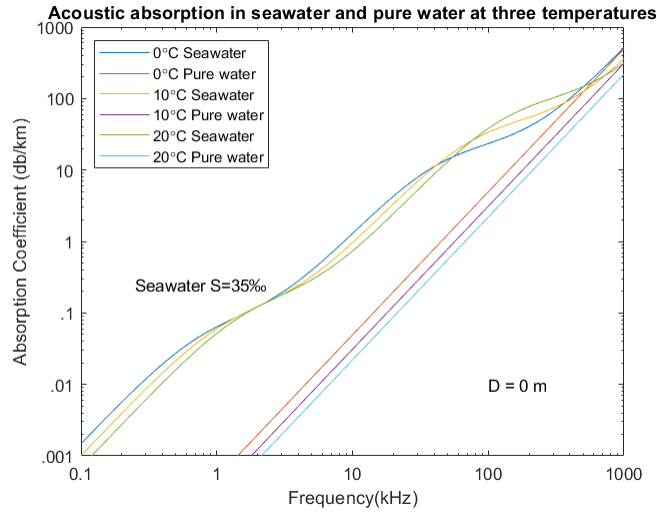
Figure 3-1: Two-dimensional absorption curves for sea water and pure water based on the Francois Garrison Equations at multiple temperatures [18] [19].
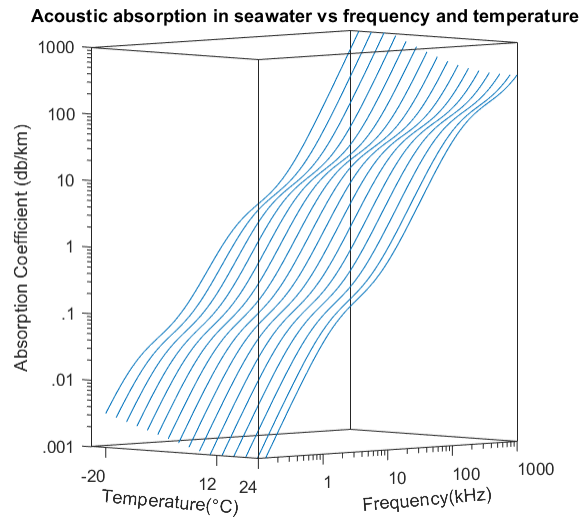
Figure 3-2: Three-dimensional representation of the absorption curves at varying frequency and temperature [18] [19].

Absorption Factors	
Factor	Dominant Frequencies
Viscous Absorption (Pure Water)	>200kHz
MgSO4	10-200kHz
Boric Acid	<10 kHz

Table 3.1: Frequency Ranges for dominant absorption factors.

The general absorption equation describes the frequency dependence of the absorption coefficient, α, based on several constants defined below:

$$\alpha = \frac{A_1 P_1 f_1 f^2}{f_1^2 + f^2} + \frac{A_2 P_2 f_2 f^2}{f_2^2 + f^2} + A_3 P_3 f^2 \tag{3.1}$$

where α has units of dB·km^{-1} [18] [19].

This equation is a sum of the three main factors impacting the absorption of sound in seawater. Each factor is assigned A, P, and f_n terms while including the frequency of interest, f. The A term was originally intended as an adjustment constant but was later determined to depend on environmental conditions. A_1 is specifically dependent on sound speed and pH and carries the units (dB km^{-1} kHz^{-1}). Subsequently, A_2 carries the same units as A_1 and is dependent on sound speed, temperature, and salinity. A_3 is associated with the pure water contribution and has units of (dB km^{-1} kHz^{-2}) due to the absorption from pure water being proportional to the square of the frequency. P_1, P_2, and P_3 serve as a pressure adjustments in order to fit curves to experimental data. The f_n terms represent a relaxation frequency calculated based on the associated element's absorption per wavelength of a given frequency. Each relaxation frequency is designated to match the contributions of that factor to absorption. The terms f_1 and f_2 carry the units (kHz). The viscous absorption factor from pure water does not have a relaxation frequency, and it displays a log-linear curve in frequency versus absorption.

The full breakdown of each term is listed below and fully described in [18] [19].

Boric Acid Factor

$$A_1 = \frac{8.86}{c} \times 10^{0.78\text{pH}-5}$$

$$P_1 = 1 \qquad (3.2)$$

$$f_1 = 2.8 \times (\sqrt{S/35}) \times 10^{4-1245/\theta}$$

MgSO₄ Factor

$$A_2 = \frac{21.44 \times S}{c}(1 + 0.025T)$$

$$P_2 = 1 - 1.37 \times 10^{-4}D + 6.2 \times 10^{-9}D^2 \qquad (3.3)$$

$$f_2 = \frac{8.17 \times 10^{(8-\frac{1990}{\theta})}}{1 + 0.0018(S - 35)}$$

Pure Water Factor

For $T \leq 20°C$

$$A_3 = 4.937 \times 10^{-4} - 2.59 \times 10^{-5}T$$
$$+ 9.11 \times 10^{-7}T^2 - 1.50 \times 10^{-8}T^3 \qquad (3.4)$$
$$P_3 = 1 - 3.83 \times 10^{-5}D + 4.9 \times 10^{-10}D^2$$

For $T > 20°C$

$$A_3 = 3.694 \times 10^{-4} - 1.146 \times 10^{-5}T$$
$$+ 1.45 \times 10^{-7}T^2 - 6.5 \times 10^{-10}T^3 \qquad (3.5)$$
$$P_3 = 1 - 3.83 \times 10^{-5}D + 4.9 \times 10^{-10}D^2$$

Note: T is temperature in °C, c is sound speed in (m/s), f is frequency in (kHz), θ is $T+273$ or absolute temperature in Kelvin (K), S is salinity in parts per thousand (‰), and D is depth in meters (m).

3.2 Assessing the Acoustics at Source and Receiver

In the mission profile considered for this thesis, a swarm of underwater vehicles consists of a leader and multiple followers. The lead vehicle is assumed to have reliable navigation in support of the overall mission, e.g., GPS, high-end INS, and Doppler velocity log (DVL). The followers are assumed to have poor internal navigation, e.g., a MEMS IMU, leading to rapid navigation error accumulation, up to 10% of distance travelled. This approach restricts the high cost to one vehicle in the swarm: by equipping the "leader" with a sound source capable of broadcasting at multiple frequencies, "follower" vehicles can estimate a relative position.

This navigation estimate is assumed to consist of two estimates based on data collected from a single hydrophone: range and bearing. The Doppler frequency shift method approximates the bearing from the follower to the leader and clarifies any spatial ambiguity associated with the range estimation for this thesis's scope. Thus, to enable follower algorithms, the range estimation must only be consistent within a bounded error. Under these circumstances, a swarm of AUVs can operate in a set geometric formation with each vehicle remaining inside an assigned sphere at a set range and bearing from the leader. A pre-planned formation determines the location of each follower's sphere, and the error associated with the range estimation from the leader dictates the size of the sphere as denoted in Fig. 3-3. In this way, AUVs can sample a volume of space without conflicting with each other and relying on the path planning of the lead vehicle.

This work focuses on estimating range from a follower to a beacon of known frequency characteristics based on the difference in transmission loss across multiple frequencies.

For notation purposes the ~ , or tilde operator is used to denote that a value is from a measurement or an estimate, and not a perfect value based on the stochasticity of the environment and associated errors in measurements.

A single hydrophone onboard each follower records the measured received level of sound ($\tilde{RL}$) at the follower vehicle. This $\tilde{RL}$ is a function of the measured source level ($\tilde{SL}$) at a reference distance from the lead vehicle, and the transmission loss (TL) along the path between the lead and follow vehicle. However, according to [53], both $\tilde{SL}$ and $\tilde{RL}$ are subject to the noise such that:
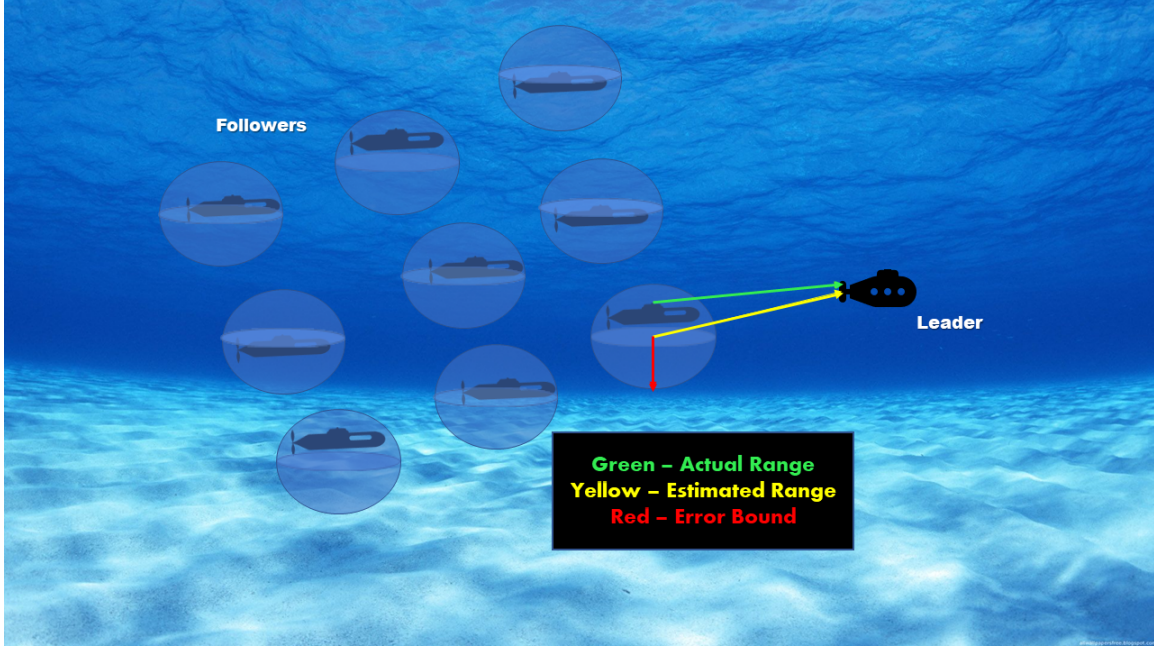
Figure 3-3: A group of AUV followers navigate relative to a leader via range and bearing estimation from Doppler shift and total transmission loss using a single-hydrophone.

$$\tilde{RL} = \tilde{SL} - TL + \tilde{N} \tag{3.6}$$

where $\tilde{RL}$, $\tilde{SL}$, and $\tilde{N}$ include any error associated with the actual measurement.

TL represents a combination of the transmission loss due to geometric spreading, absorption, and environmental scattering. Transmission loss due to geometric spreading will be based on range, and the depths of the source, receiver, and water column. However, the absorption coefficient, α, remains directly dependent on frequency and has units dB/km such that: $TL = TL_{geom} + \alpha r$. Figure 3-5 shows graphically via environmental models that, when calculating the total transmission loss minus the geometric spreading loss, the remainder is a log-linear function of range.

For clarity, using [22] and [21] as a guide, intensity, I, at a given point in space supports the derivation for the transmission loss. I is defined as:

$$I = \frac{|p|^2}{\rho c} \tag{3.7}$$

where ρ is the water density, and c is the sound speed.

The rate of loss due to absorption, i.e. due to the heat loss to the particles in the medium,

is modelled as an exponential loss factor.

$$\Delta I = I(r + dr) - I(r) = -a(I(r))dr \tag{3.8}$$

$$\frac{dI}{dr} = -a(I(r)) \tag{3.9}$$

$$I(r) = I_0 \cdot r^{-2} e^{-ar}. \tag{3.10}$$

For spherical spreading, Equation 3.9 is adapted to include the inverse square of the radius. [22]. Transmission loss is then described as the ratio $I_0/I(r)$ in dB:

$$TL = 10\log\frac{I_0}{I(r)} = 20\log\frac{I_0}{I(r)} + 10\log(e^{-ar}). \tag{3.11}$$

However, TL with absorption can also be derived by examining the more basic form for geometric spreading in a lossless medium as proportional to the inverse square of the radius for omni-directional point sources, beginning with the formula for pressure.

$$p(r, t) = \frac{A}{r} e^{j(kr-\omega t)} \tag{3.12}$$

$$|p|^2 = \frac{A^2}{r^2}. \tag{3.13}$$

This equation, however, ignores the contribution from absorption along that path in a lossy homogeneous medium. Using 3.7 and 3.10 the square modulus of the pressure is represented as:

$$|p|^2 = \rho c I = I_0 \cdot r^{-2} e^{-ar}. \tag{3.14}$$

The magnitude of the pressure including absorption is obtained by substituting 3.13 for p and maintaining the absorption factor,

$$|p|^2 = \frac{A^2}{r^2} e^{-ar} \tag{3.15}$$

$$p(r, t) = \frac{A}{r} e^{j(kr-\omega t)} e^{-ar/2}. \tag{3.16}$$

This description of pressure from the combined impacts of geometric spreading loss and environmental absorption is utilized to reevaluate the sound pressure level. Simplifying

with logarthmic rules and ignoring noise contribution:

$$SPL = 10\log\frac{|p|^2}{|p_{ref}|^2} = 10\log(\frac{A^2}{r^2 p_{ref}^2}e^{-ar})$$

$$= \underbrace{20\log\frac{A}{r_{ref}p_{ref}}}_{\text{source level}} - \underbrace{(20\log\frac{r}{r_{ref}} + ar(10\log(e)))}_{\text{transmission loss}}. \qquad (3.17)$$

Transmission loss is then calculated as a combination of geometric spreading and transmission loss.

$$TL = \underbrace{20\log\frac{r}{r_{ref}}}_{\text{Geometric Spread}} + \underbrace{ar(10\log(e))}_{\text{Absorption}}. \qquad (3.18)$$

For the absorption term the more common notation in which the constant a is combined with $\log(e)$ into the absorption coefficient α, a 10^{-3} factor is added since α is in units of $\frac{dB}{km}$,

$$ar(10\log(e)) = \alpha r(10^{-3}).$$

3.2.1 Geometric Spreading Loss

While the assumption of spherical spreading allowed for simplicity, the geometric spreading loss is a combination of spherical and cylindrical spreading based on the distance at which the signal meets the surface and bottom boundaries. For example, if the water column depth is 100 m, the source depth is 50 meters, and $r_{ref} = 1$ meter the geometric spreading loss at 1 km is calculated as:

$$TL_{geom} = \underbrace{10\log(\frac{1000}{1})}_{\text{Cylindrical Spreading}} + \underbrace{(20\log(\frac{50}{1}) - 10\log(\frac{50}{1}))}_{\text{Addition from Spherical Spreading}}.$$

3.3 Environmental Models and Transmission loss

The next step is to evaluate the total transmission loss in various environments. Simulation-based environmental modeling demonstrates the feasibility of SABRE in multiple environments. Environmental modelling gives insight into the contributions of different aspects of transmission loss: six environments with varying depths, listed in Table 3.2, were modelled using BELLHOP [23].

Environment	Depth	Range	Source and Receiver Depth	Sound Speed Profile
1	3 m	10 km	1.5 m	Constant
2	10 m	10 km	5 m	Constant
3	100 m	10 km	50 m	Constant
4	500 m	10 km	250 m	Munk
5	1 km	10 km	500 m	Munk
6	5 km	10 km	2.5 km	Munk

Table 3.2: List of Environmental Model Parameters
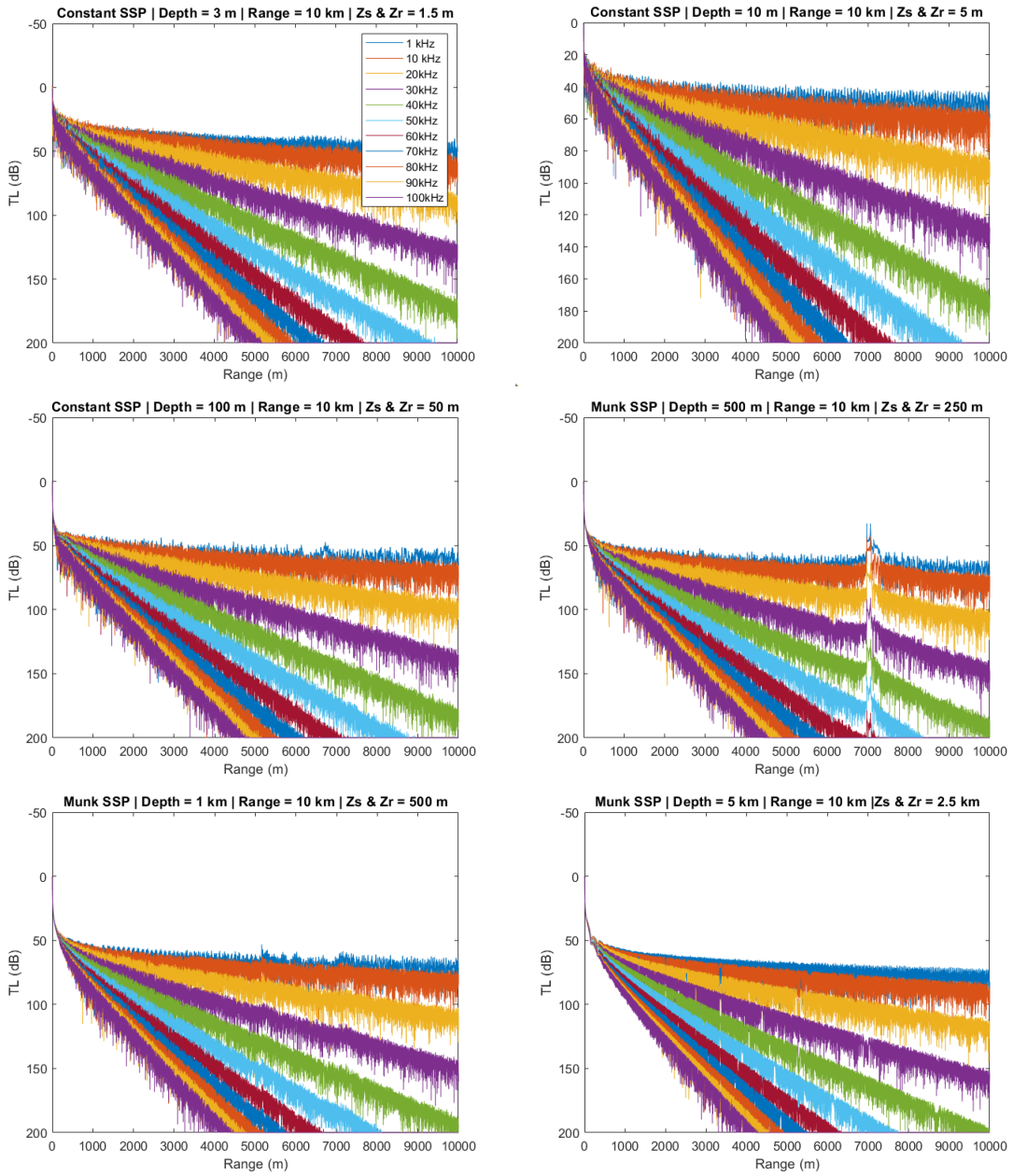
Figure 3-4: Transmission Loss Models for varied Environments

BELLHOP models do not account for environmental parameters that impact absorption, such as temperature, salinity, and pH, and are expected to reflect solely geometric spreading loss. However, analysis of Environment 6 with 5 km in-depth, a Munk sound speed profile, and source/receiver depths of 2.5 km indicates otherwise. For this environment, the geometric spreading is spherical out to a range equal to the receiver's depth and cylindrical, spreading beyond that based on the water column acting as a waveguide [20]. This approach is equivalent to modeling the entire distance as a cylindrical spread and adding the dB difference from the first 2.5 km of spherical spreading. The sound source and the receiver depths in the middle of the water column allow for this convenient calculation. This environmental model also has the least amount of loss due to scattering and multipath effects based on the selected depth and range for the source and receiver.

$$TL_{spherical} = 20\log(r) \approx 68.0 \text{ dB, for spherical spreading out to 2500 m}$$

$$TL_{cylindrical} = 10\log(r) \approx 34.0 \text{ dB, for cylindrical spreading out to 2500 m}$$

$$TL_{spherical} - TL_{cylindrical} \approx 34.0 \text{ dB, difference at 2500 m}$$

$$TL_{geom} \approx 10\log(r) + 34.0, \text{ total geometric spreading loss for distances} > 2500 \text{ m}$$

It is apparent that BELLHOP models account for transmission loss beyond geometric spreading when comparing the calculations at 10 km in Table 3.3. Absorption coefficients are calculated based on assumed values for temperature ($T = 15°C$), salinity ($S = 35$ ‰), and $pH = 8$. The frequency-based calculation from [20] and [21] for attenuation is included in this comparison based on the assumption that the BELLHOP output is this estimate plus an added noise and loss from interaction with surface and bottom boundary layers. The frequency-only estimation does not account for environmental parameters, but instead provides a simpler estimate via:

$$\alpha' \simeq 3.3 \times 10^{-3} + \frac{0.11f^2}{1 + f^2} + \frac{44f^2}{4100 + f^2} + 3.0 \times 10^{-4}f^2 \text{ (dB/km)} \qquad (3.19)$$

This comparison highlights that while the formulas used to estimate absorption are different, there is consistency in their frequency dependence. The Francois-Garrison equations will provide superior accuracy to the non-environmentally dependent BELLHOP model, as
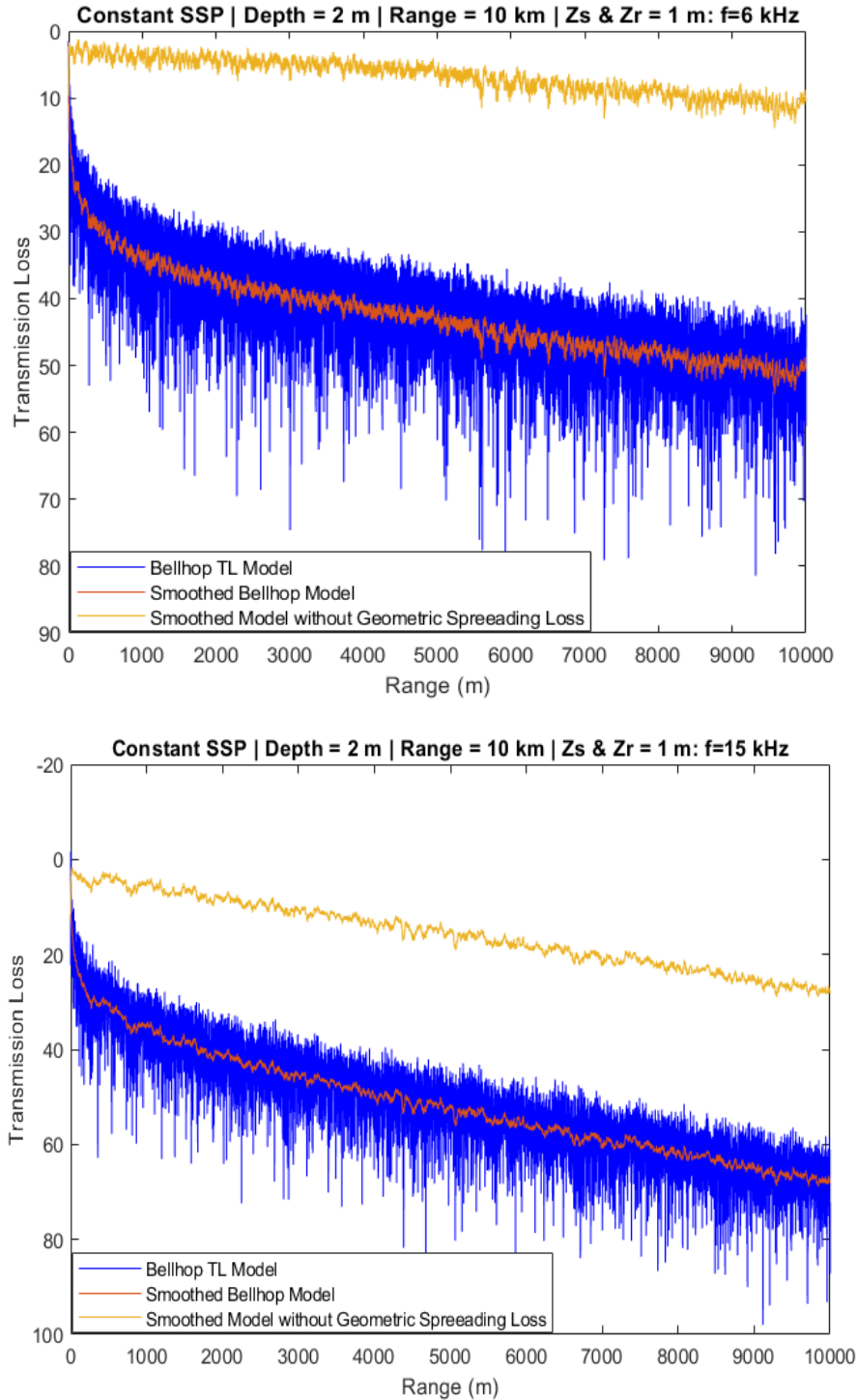
Figure 3-5: The model estimates transmission loss for a very shallow environment at 6 and 15 kHz. BELLHOP's output for transmission loss is smoother using a moving mean prior to subtracting the loss attributed to geometric spreading. The log-linear curve that results when geometric spreading loss is removed supports the assumption that the difference in transmission loss will allow comparison of log-linear absorption functions. This environmental model will be discussed in more detail in Chapter 4.

f	Spreading (dB)	α	Total (α)	Total(α')	BELLHOP (dB)
1 kHz	74.0	0.053	74.5	74.7	72.3
10 kHz	74.0	0.612	80.1	85.9	85.0
20 kHz	74.0	2.007	94.1	115.4	128.4
30 kHz	74.0	4.169	115.7	157.0	152.24
40 kHz	74.0	6.902	143.0	203.4	205.7
50 kHz	74.0	9.998	174.0	249.3	243.7
60 kHz	74.0	13.267	206.6	291.6	288.9
70 kHz	74.0	16.562	239.6	329.4	322.8
80 kHz	74.0	19.779	271.8	362.5	338.0
90 kHz	74.0	22.855	302.5	391.5	367.5
100 kHz	74.0	25.758	331.6	417.2	393.7

Table 3.3: Comparing TL over 10 km from Francois-Garrison, frequency-only estimates, and BELLHOP models

is stated in [20]. However, Figure 3-5 shows the log-linear curve that results when the environmental model is smoothed, and geometric spreading loss is removed. These log-linear curves are the environmental model's estimated loss to absorption.

3.4 Formulating Range Estimations

The first observation is that geometric spreading is frequency independent, and the frequency dependence in the models comes from absorption, scattering, and multipath effects. Acoustic absorption is modelled versus frequency similarly in Figure 3-6, which shows a log-linear behavior at all ranges in each environment. Environments and frequencies that minimize multipath are optimal the only model for these effects must be extracted from BELLHOP and accuracy will suffer in extreme environments. However, it is notable that increased source and receiver depths slightly decrease the transmission loss due to absorption according to [18] [19]. The difference in absorption between frequencies also decreases as depth increases according to the pressure contribution in the Francois-Garrison equations. These impacts are minimal at frequencies below 10 kHz, but are more notable at higher frequencies. For example, at 10 kHz the absorption at a 10 meter depth is about 0.1 dB greater than at a 1 kilometer depth. However, at 40 kHz the difference is 1.4 dB, and at 100 kHz it rises to 3.7 dB. This is important to note as it impacts the difference in absorption between the two frequencies and at significant depth their separation may be decreased, but those depths will still be desirable if they mitigate multipath effects. Absorption coefficients
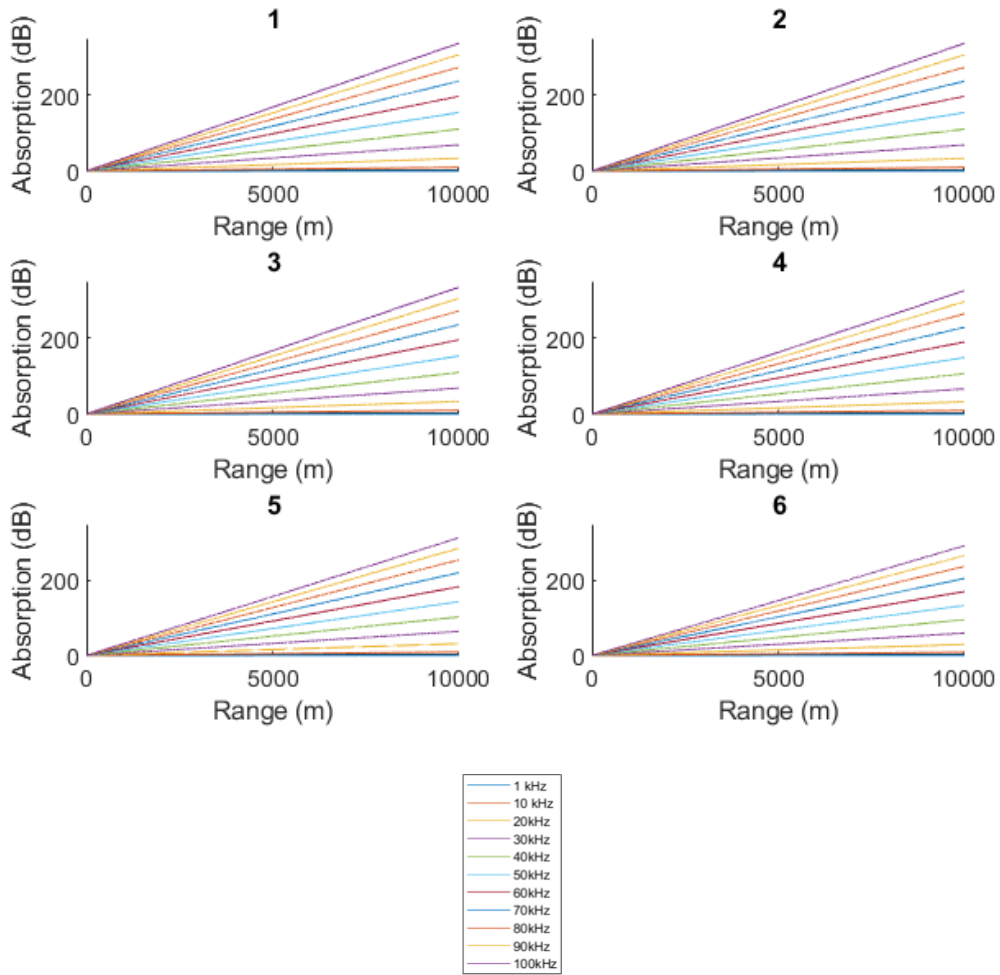
Figure 3-6: Absorption Models

that are too close together will be more sensitive at closer ranges as minor fluctuations in RL will indicate significant shifts in the range estimate.

Separating geometric spreading as frequency independent:

$$\Delta RL = RL_{f_1} - RL_{f_2} = SL_{f_1} - TL_{f_1} + N_{f_1} - (SL_{f_2} - TL_{f_2} + N_{f_2})$$
$$= (SL_{f_1} - TL_{geom} - \alpha_{f_1}r + N_{f_1}) - (SL_{f_2} - TL_{geom} - \alpha_{f_2}r + N_{f_2})$$
$$= SL_{f_1} - \alpha_{f_1}r - SL_{f_2} + \alpha_{f_2}r + N_{f_1} - N_{f_2} \quad (3.20)$$

and range is calculated through ΔRL.

$$r = \frac{\Delta RL + SL_{f_2} - SL_{f_1} - N_{f_1} + N_{f_2}}{\alpha_{f_2} - \alpha_{f_1}} \quad (3.21)$$

It remains feasible to estimate range directly from a single frequency, but that estimation would include geometric spreading loss. Since geometric spreading loss does not follow a log-linear trend until a set range, a single frequency estimation will be more sensitive to error, especially at shorter ranges. Using the difference in total transmission loss at two frequencies the goal is to remove the loss from geometric spreading and assess range in terms of two log-linear, frequency-dependent functions. Frequencies with adequate separation in their absorption rates are ideal to maximize the detectable difference in total transmission loss between the two.

In the case in which the source level at a particular frequency is unknown, and assuming that the source level does not fluctuate considerably, estimation is based on a change in the range between measurements at a single hydrophone via ΔRL.

$$r_2 - r_1 = \frac{\Delta RL_2 - \Delta RL_1}{\alpha_{f_2} - \alpha_{f_1}} \quad (3.22)$$

In this way, if it is feasible to establish an initial range measurement for a follower vehicle, then future range estimates can be based on that reference. This method is sensitive to fluctuations in the sound level at the source and assumes that the reference point chosen is reliable. There are also potential sensitivities to environmental mismatch and multipath effects.

3.5 Evaluating Factors for Estimation Accuracy

The selection for α and measured sound levels are assumed to be accurate, but in reality, there will be some error in comparison to the actual absorption and sound level values, and it will vary in space and time. These errors must be accounted for and understood to determine their impact on the range estimate. The error associated with the range estimate includes any errors in calculating the difference in received sound level. These errors will include the absorption coefficients and noise in the measurements. The calculation of the received sound level takes into account; the source level (SL), the transmission loss (TL), and the ambient noise (N) at each frequency.

An average measurement at reference range (r_{ref}) represents the measured source level. The received level is determined based on the data received at the single hydrophone onboard the follower AUV and is subject to the error associated with this instrument. Measurements during periods in which the source is not transmitting represent measured noise levels. The source's far field is represented by

$$r > \frac{L^2}{\lambda} \tag{3.23}$$

where L is the length of the source aperture and λ is the wavelength of the signal. This is important to ensure our reference distance and measurements are consistent based on the far field assumption.
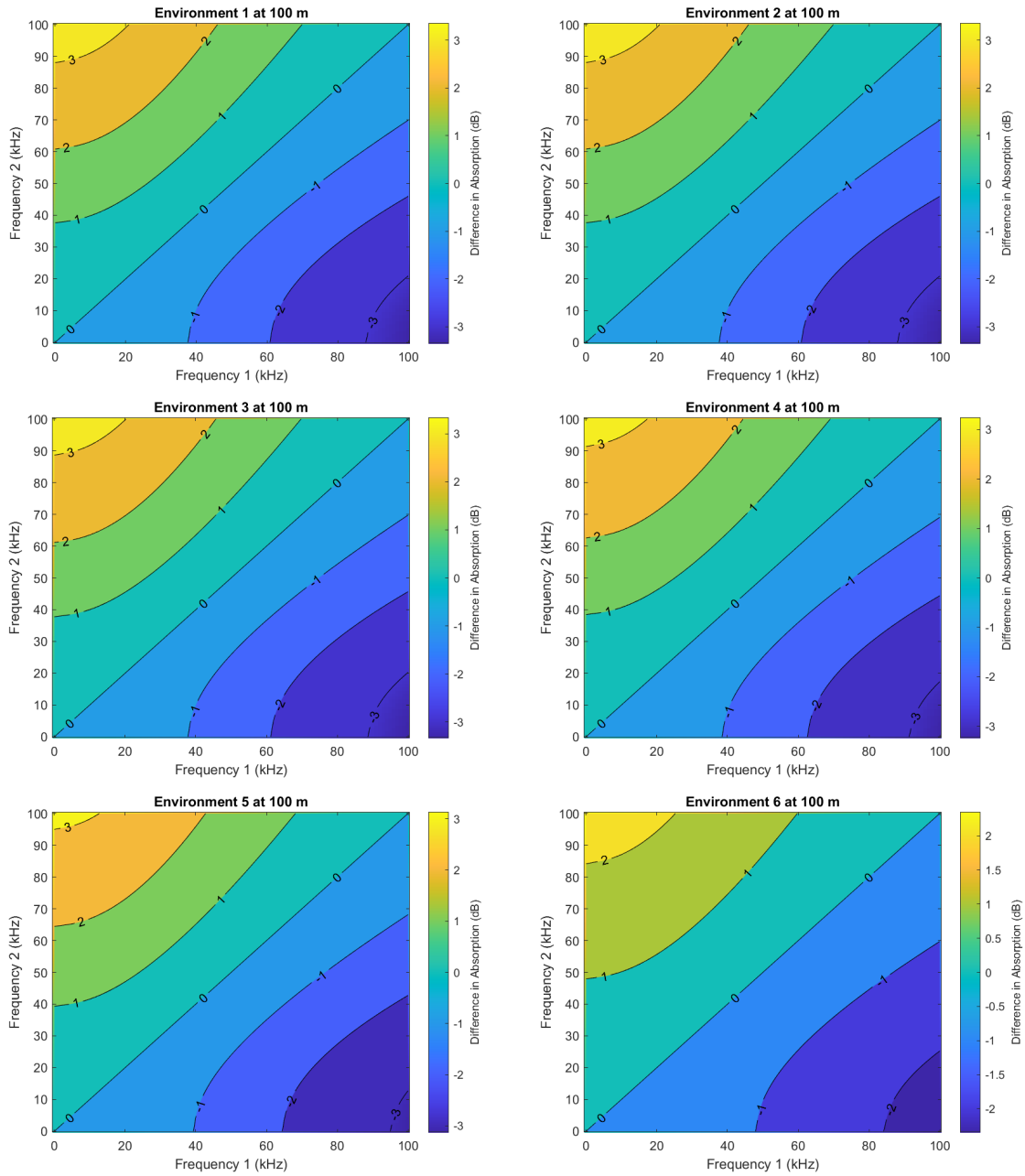
Figure 3-7: Differential frequency Transmission Loss at 100 meters.
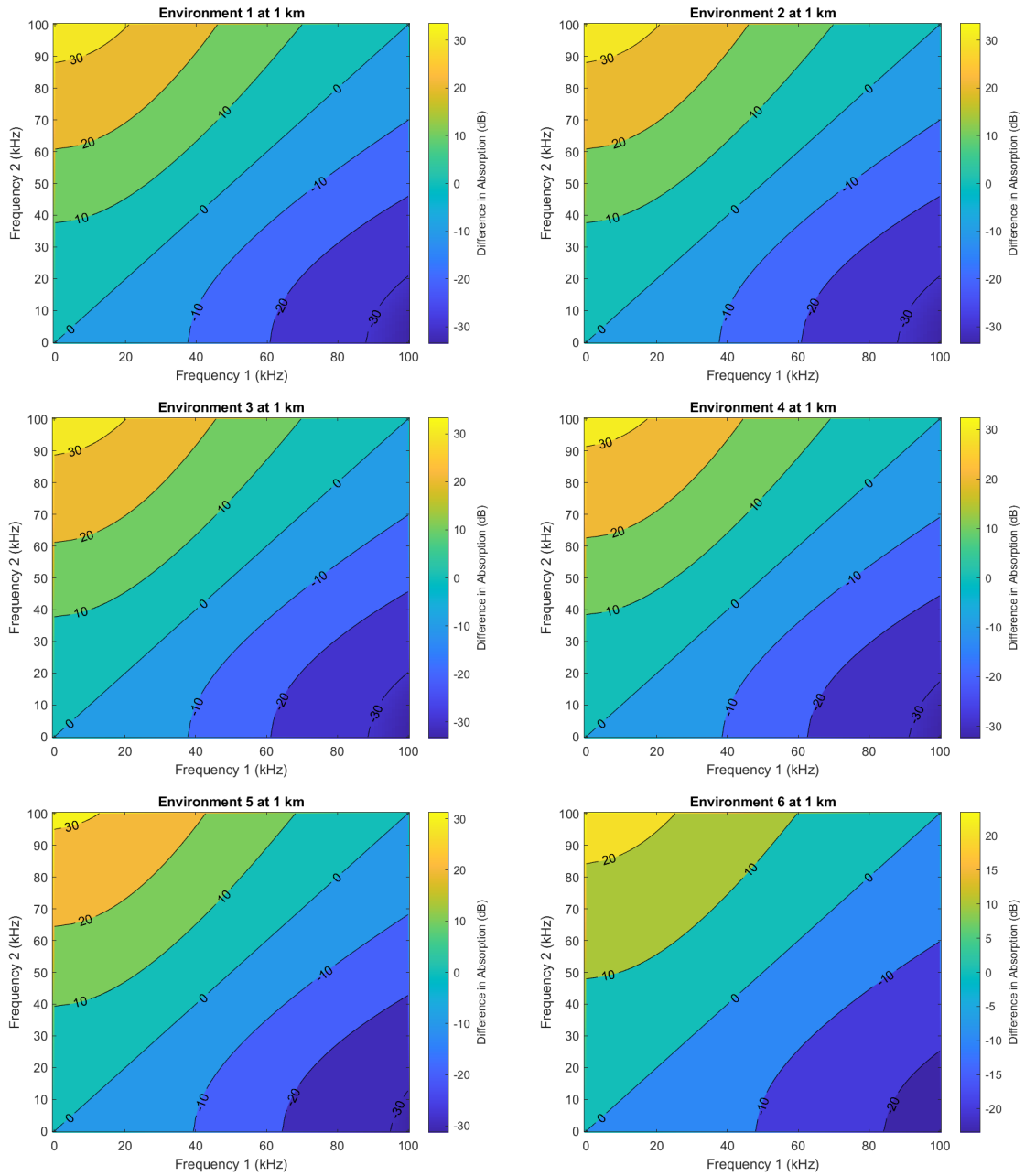
Figure 3-8: Differential frequency Transmission Loss at 1 km.

Calculations for the difference in TL at two frequencies at distances of one hundred meters and one kilometer in various environments identify the separation in dB attainable at different frequency pairings. Figures 3-7 and 3-8 display how this difference grows with the separation of frequencies based on their different absorption coefficients. The difference in coefficients represents the difference in absorption-based transmission loss over 100 meters and one kilometer respectively. This analysis allows us to choose frequencies based on an assessment of the environment, hardware limitations, and operational requirements. The frequencies selected must support the desired ranges and have enough separation to provide a discernible difference in received sound level at a single hydrophone. Therefore the pre-mission assessment should take into account the source level, potential noise levels, calculated transmission loss, and calculated difference in transmission loss at each frequency. This last consideration will determine detection range as increased separation of frequencies will have an increased rate of change in ΔRL while closer frequencies will require longer ranges to provide a consistent difference in transmission loss.

$$\tilde{r} = \frac{\Delta RL + S\tilde{L}_{f_2} - S\tilde{L}_{f_1} - \tilde{N}_{f_1} + \tilde{N}_{f_2}}{\hat{\alpha_{f_2}} - \hat{\alpha_{f_1}}} \tag{3.24}$$

where $\hat{\alpha_{f_2}}$ and $\hat{\alpha_{f_2}}$ are estimates for absorption with some associated error when compared to the actual absorption in the environment. Equation 3.20 allows substitution for ΔRL based on the actual values for SL, N, and α at each frequency. $\tilde{r}$ is left as a function of the error in each term, the actual absorption coefficients for the environment, and range:

$$\tilde{r} = \frac{\varepsilon_{SL_2} - \varepsilon_{SL_1} - \varepsilon_{N_1} + \varepsilon_{N_2} + (\alpha_{f_2} - \alpha_{f_1})r}{\hat{\alpha_{f_2}} - \hat{\alpha_{f_1}}} \tag{3.25}$$

The measured sound levels at the source and hydrophone onboard the follower vehicle are sources of error in this range estimation. Also, the absorption coefficients and model for spreading loss at each frequency are estimations containing some error. The goal is to identify the bounds of that error within ranges that support the detection of two distinct frequencies from the source. The errors in measured sound level are combined into one error term, η, so the range estimation's sensitivity to the accuracy of the absorption coefficients may be assessed.

$$r - \tilde{r} = r - \frac{\eta + (\alpha_{f_2} - \alpha_{f_1})r}{\hat{\alpha_{f_2}} - \hat{\alpha_{f_1}}} \tag{3.26}$$

The sensitivity to an error in α is assessed by selecting prospective frequency pairings and determining the total transmission loss and range estimation impact. The difference in transmission loss at frequencies from 10-100 kHz in the six environmental models at 100 meters and 1 km in range informs options for frequency pairings. Based on Figure 3-7 and 3-8 plots, 10 kHz and 40 kHz present a good prospect for frequency pairing due to the significant separation while maintaining frequencies that can still broadcast distances in kilometers. This pairing will perform well at maximum source depths, as these will be significantly less than Environment 6 for nearly all sound sources. The goal will be to optimize the transmission range of the frequencies while mitigating multipath wherever possible.

If absorption in the environment is greater than the estimated absorption coefficient, $\alpha > \tilde{\alpha}$, then $r < \tilde{r}$ and vice versa. While the differences between each α at a selected frequency may vary, it is expected that if $\tilde{\alpha_{f_1}}$ is underestimated, the same will be true for $\tilde{\alpha_{f_2}}$. SABRE's sensitivity is assessed by plotting the impact of errors in α in Figure 3-9. Interestingly, if α_1 and α_2 are over or underestimated by approximately the same amount, the error in range will be minimal. However, any misestimations will likely differ in magnitude due to the selection of widely separated frequencies.

Range estimations will become less reliable at ranges where the signal to noise ratio (SNR) approaches zero, e.g. $RL = N$. It is near these ranges that the noise estimate becomes most important. This transition is critical because a low estimate of the noise will cause range estimations to continue after the pressure contribution of at least one frequency has dissipated. For this reason, a conservative estimate for ambient noise is advisable, and at that threshold, SABRE will cease to provide reliable estimations. This threshold integrates into SABRE's feedback control loop to maintain minimum distances to continue range estimation or shift to an alternate navigation method until estimations return to a reliable threshold.

For example, at a given frequency, if $RL = SL - TL + N$ and calculations for SL are from the source's sound pressure at a reference distance, then the limit on SABRE's range is at $TL = SL$. This limit exists because beyond that range $RL = N$, ΔRL would be a function of the ambient noise, precluding range estimation. If the estimate for noise were lower than the actual noise, range estimates would continue after reaching the noise threshold and would be assumed valid while the target's actual range could continue to change unpredictably.
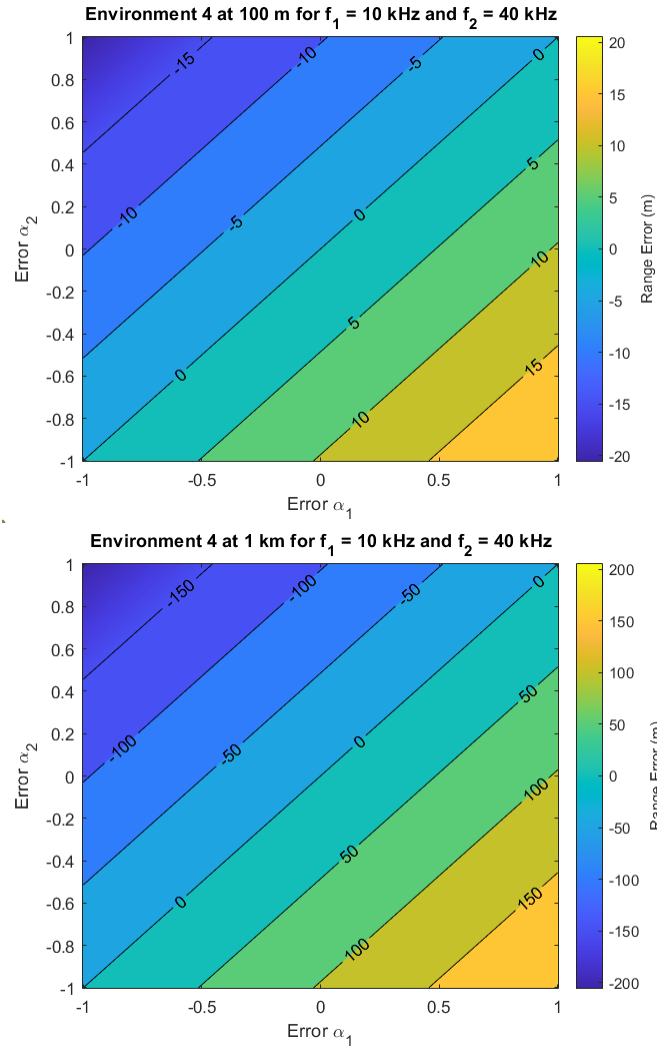
Figure 3-9: Errors in α show a linear impact with range as expected. A frequency pairing of 10 kHz and 40 kHz in Environment 4 maximizes frequency separation in an environment deep enough to mitigate multipath. Real-world experiments will evaluate whether the proposed depths are sufficient.

3.6   Summary

This chapter reviewed the empirical equations used to calculate the absorption coefficient, α, for a particular frequency and set of environmental conditions. The units for α are dB/km.

The derivation for the transmission loss is shown through the acoustic intensity and pressure at the source and receiver, highlighting the difference between an assumed lossless medium and a lossy homogeneous medium. Transmission loss is treated as a combination of geometric spreading loss and losses to absorption.

We also covered several environmental models that aid analysis on the environments in which SABRE is anticipated to provide reliable estimates and environments that will be more difficult due to increased impacts from multipath.

Lastly, we proposed a mathematical method for estimating range based on the difference in transmission loss at two frequencies. The chapter closes with an evaluation of the sources of error and sensitivity within this estimation.

Chapter 4

Experimental Protocols and Data Processing

This chapter provides an overview of the equipment used, testing procedures, and experimental protocols. It includes a review of the signal processing techniques used to estimate range via the differential frequency transmission loss, and provides initial results from SABRE in the experimental environment. The goal for equipment testing and follow-on experimentation was to verify amplitude estimations methods as a means to support range estimation.

4.1   Experimental Setup

Prior to data collection the first goal was to test the equipment setup to demonstrate amplitude estimation at short static ranges prior to conducting field trials. Initial data collection focused on simplicity and addressed hardware limitations and environment access due to COVID-19. The hardware used was the best equipment available on short notice before quarantine measures took effect. However, a positive outcome from these limitations was demonstrating that feasibility assessments for SABRE were not personnel-intensive. Initial experiments required only a single operator and a non-participating safety observer. Experiments were feasible due to private dock access on Bourne Pond, a tidal pond area in East Falmouth, MA.

4.1.1 Equipment

Equipment	Purpose	Specifications/Limitations
2 HTI-96-Min Hydrophones	Receivers	2 Hz-30 kHz
USB-1608FS-PLUS DAQ	Data Recording	Sample Rate 100 kS/s
Raspi3	Data Storage	16 GB SSD
Laptop	Dual-tone signal	Limits source depth
Kayak	Mobilize Receiver	Human Operator
Garmin inReach Explorer	GPS Ranges	Irregular sampling
Lubell LL916C	Sound Source	0.5-21 kHz, 18 m depth 0-41°C

Table 4.1: Equipment for Initial Data Collection

4.1.2 Preparation

During the complete shutdown for COVID-19 restrictions, equipment preparation and testing was still feasible at home. Once acquired, the equipment in Table 4.1 was tested at home, utilizing a deep bathtub. The intent was not to test SABRE's performance, but instead to ensure that the setup would adequately play and record data at the predetermined frequencies should the opportunity for real-world data collection become available. The setup is pictured below in Figure 4-1.
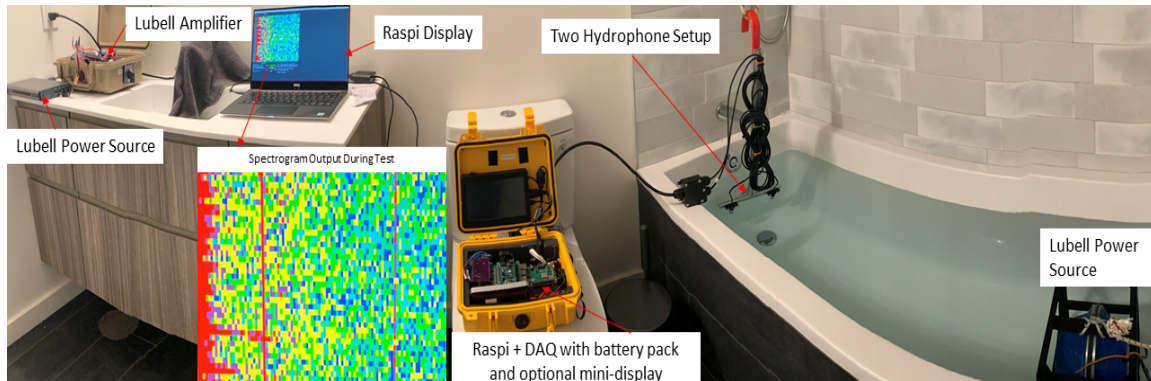
Figure 4-1: Equipment Setup for system tested during COVID-19 Stay Home advisory in preparation for Data Collection.

Dual-frequency tones were created in MATLAB using a sine wave at the desired frequencies, as in Equation 4.1. The amplitude, A, was adjusted to avoid data clipping during tone creation in MATLAB. The tone was played via laptop headphone jack to a Lubell LL916-C-025 underwater speaker system. Two hydrophones attached to a USB digital acquisition (DAQ) system and Raspberry Pi recorded received signal at each hydrophone. Only a single hydrophone is necessary, but two allowed for redundancy if one of the channels were to perform poorly. This testing verified the equipment setup before transiting to the data collection site and provided information on frequency selection and data acquisition. A dual-frequency tone at 6 kHz and 15 kHz was selected based on the frequency limitations of the source and anticipated noise bands in the experimental environment. At these frequencies and environmental conditions, the difference in absorption rates is under 2 dB/km. The goal was to achieve 3 dB of separation in absorption for the desired range [14]. Given that the range in this experiment was approximately 230 meters, there is only a small difference in absorption loss for the frequency pairing of approximately 0.5 dB at maximum range, and even less at shorter ranges. 15 kHz is the highest frequency selected due to the assessment that the source would not perform as reliably near the high end of its frequency range. 6 kHz is the lowest frequency selected due to concerns that there would be increased noise in the environment at lower frequencies. This testing setup provided valuable feedback before field deployment, but one drawback was that the hydrophones became saturated at higher volume tones due to the proximity of the source and receiver, and multiple reflective boundaries in the testing tub.

$$x[t] = A \cdot sin(2\pi f_1 t) + A \cdot sin(2\pi f_2 t) \tag{4.1}$$

The equipment referenced in Table 4.1 was then relocated to East Falmouth for testing in Bourne Pond. Two hydrophones were attached onboard a single-person kayak and connected to a USB digital acquisition device and Raspberry Pi to record received signals at each hydrophone. An Adafruit Breakout GPS and Garmin inReach Explorer Plus Handheld GPS record the kayak and hydrophone positions throughout data collection. The Garmin GPS provides primary ground truth position, and the Adafruit GPS is for redundancy.

This experiment's goal was to demonstrate SABRE by measuring source level at a one-meter static reference distance, using periods without signal for noise estimation, and vary

Time (UTC)	Event	Purpose
10:24:30	GPS, DAQ, Hydrophones ON	Noise Collection
10:29:30	Dual Tone 6/15 kHz ON	Source Level at Reference Distance
10:30:30	Dual Tone OFF	Create gap in signal prior transit
10:31:30	Dual Tone ON	Data Collection with variable range
10:31:30-10:55:40	Transit to 230 m and return	Increase/Decrease range to source
10:55:40	Dual Tone OFF	Noise collection
10:56:38	GPS and DAQ OFF	Experiment Complete

Table 4.2: Sequence of Events for May 14, 2020 Experiment

Parameter	Value	Justification
Salinity	25 ‰	June 15, 2020 CTD Measurement
Temperature	$5°C$	Estimated
pH	8.0	Estimated
Depth	2 meters	Estimated
Source and Receiver Depth	1 meter	Measured
Dual-tone Generator (F_s) Sampling Frequency	44.1 kHz	Selected
Dual Tone (f_1/f_2)	6/15 kHz	Selected

Table 4.3: May 14, 2020 Experiment Parameters

the range to the source via an out and back transit denoted in Figure 4-2. This experimental protocol succeeded in providing relevant data, but also provided numerous lessons-learned for subsequent protocols.

For clarity, the timeline in Table 4.2 and pictured in Figures 4-2 and 4-4 details the events in chronological order. On May 14, 2020, the referenced equipment arrived at a private dock on Bourne Pond in East Falmouth, MA. An audio jack connects the laptop with the preloaded dual-frequency tone connected to the sound source. The two hydrophones attached to the kayak bow. The front passenger area of the kayak housed the Raspberry Pi, DAQ, and mini display screen. An external lithium-ion battery pack powered the Raspberry Pi, and the DAQ. Hydrophone recording was activated via Linux Command Line to begin recording ambient noise for one minute. A real-time command-line spectrogram verified noise collection and monitored received signal throughout the experiment. The sound source remained on the dock during noise collection periods. A one-meter reference distance marked the position for the Lubell sound source relative to the hydrophones. The dual-tone frequency was turned on for one minute to establish the reference source level for future calculations. The sound source was deactivated and removed from the water for one minute
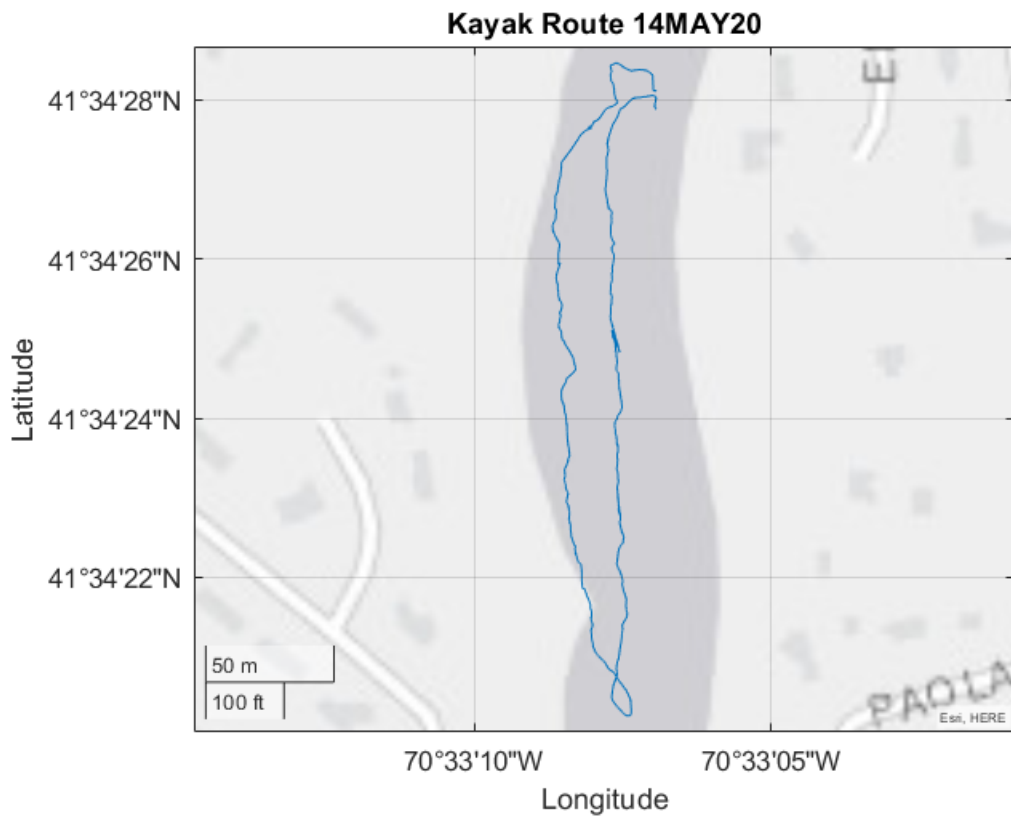
Figure 4-2: GPS track for May 14, 2020 Data Collection

to create an identifiable gap in the signal before commencing the kayak transit. After one minute, the sound source reentered the water at the same location and depth. The signal was activated, and the kayak began the transit to approximately 230 meters south then return to its start location. The sound source was deactivated and removed from the water, but hydrophones continued to record for approximately one minute without signal to identify the end of the transit.

The sampling rate and signal details relevant to the experimental protocol are in Table 4.3. The data sampling rate, F_s, was set at 44.1 kHz to satisfy the Nyquist frequency for the 15 kHz portion of the dual-tone.

$$F_s \geq 2 \cdot f_{max} \tag{4.2}$$

The sample rate is over twice the rate of the highest band-limited frequency reconstructed without aliasing [24].

4.2 Signal Processing

4.2.1 Data Parsing and Frequency Content

After the experiment, the Raspberry Pi uploads files for further analysis. The sampling rate on the DAQ records .txt files that are one second in length and contain 44,100 samples per file. To reconstruct the time series files are imported into MATLAB to form a two-channel array of samples. One channel's data is isolated to focus on a single hydrophone.

The details for the initial data and subsequent revisions are present in Table 4.4. The first step is to trim the data to remove extraneous recordings caused by the latency between the actual stop recording time, and the last file recorded. This lag results in sections of data, particularly at the end of the experiment, with zero values that become problematic if not removed due to the desire to assess received sound levels on a log scale. Data from

Data	Size	Details
All Hydrophone Data	83745900×2	2-channel data recorded on DAQ
Trimmed Data	82246500×1	Channel 2 Recorded Data
Data Snapshots	44100×1860	Averaging in Time Snapshots
RL per Bin Width	1764×1860	25 Hz Frequency bands

Table 4.4: May 14, 2020 Data Collection Details

channel two is analyzed, though both channels record similar outputs.

Figure 4-3 shows the trimmed data as the raw output from the hydrophones in a row vector. The vector length and GPS data time stamps show that the two timelines are synchronized.
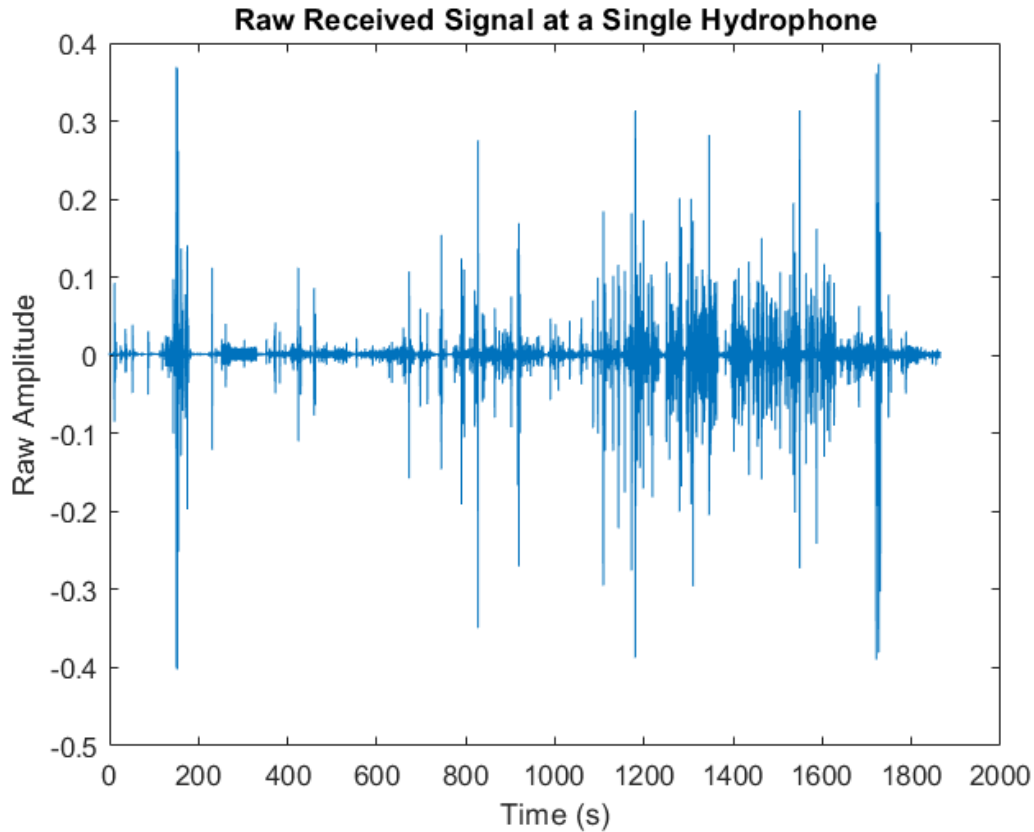
Figure 4-3: Raw Data on a Single Hydrophone for MAY 14, 2020 Data Collection

This data is the response to the system, or $y[t]$. The next step is to reshape this data from an $F_s \cdot t$ length vector into a matrix with dimensions F_s and t, where t is time in seconds. In this way, the data forms a matrix that contains one second of data per column with each row representing a specific sample from that second in time. The Fourier Transform reconstructs the frequency content in $y[t]$, or computationally, the Discrete Short-Time Fourier Transform, which uses the Fast Fourier Transform and a sliding frame over the time series to create a spectrogram [24].

$$Y[e^{j2\pi f}] = \sum_{t=0}^{\infty} y[t] \cdot e^{-j2\pi ft} \tag{4.3}$$

Graphically there is interest in $10 \cdot \log |Y[e^{j2\pi f}]|$, where log is the base 10 logarithm of the argument, but the main focus is the power spectral density (PSD),

$$PSD = 10 \cdot \log |Y[e^{j2\pi f}]|^2 \qquad (4.4)$$

and plot the results in Figure 4-3 as a heat map [24]. The different plots for the PSD represent variations in snapshot length, frequency bin size, and normalization. Snapshots in time can address peaks and valleys in signal strength by averaging over variable time lengths. Frequency bin widths allow us to broaden or narrow frequency bands to capture the energy that may be associated with frequencies some Δf from f_1 or f_2. This technique may be more or less appropriate depending on the main lobe's width at a frequency of interest. These tools can also allow for more efficient computation when dealing with large amounts of data. The average of multiple columns yields longer snapshots in time, and averaging across rows produces a wider bin width for frequency.

The received signal content displayed in the spectrogram shows the experimental timeline in Figure 4-4.

The different versions of the spectrogram provide details on the received signals, but also relevant information on ambient noise. The 6 kHz band is subject to significantly higher ambient noise with an identifiable noise band between 5 and 7.5 kHz, and intermittent high levels of broadband noise, particularly at frequencies less than 10 kHz. There is a wide main lobe at the 6 kHz frequency, and significant fluctuations in RL at close ranges, which create issues in the subsequent analysis and range estimation. This impact is particularly noticeable at 15 kHz during the outbound transit. However, the phenomenon does not replicate itself during the return transit. This disparity is potentially due to the multipath or the pose of the kayak relative to the sound source.

4.2.2   Exploring the Signals at 6 and 15 kHz

Investigation after this experiment showed several potential contributors to the poor resolution at 6 kHz and fluctuations in RL at 15 kHz during the outbound transit, the choice in frequency, and the method for powering the sound source, and the impacts of the shallow water environment.

Additional analysis of the frequency choice revealed a potential issue with operating the
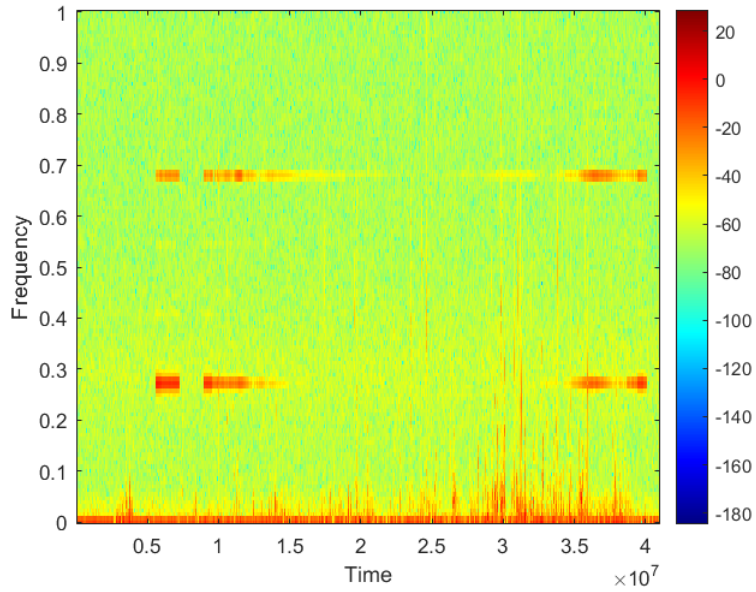
Figure 4-3a: Spectrogram a) shows normalized frequency range such that $\frac{f}{f_{max}}$ creates a scaled frequency axis from zero to one and the output is scaled from -180 to 20 dB
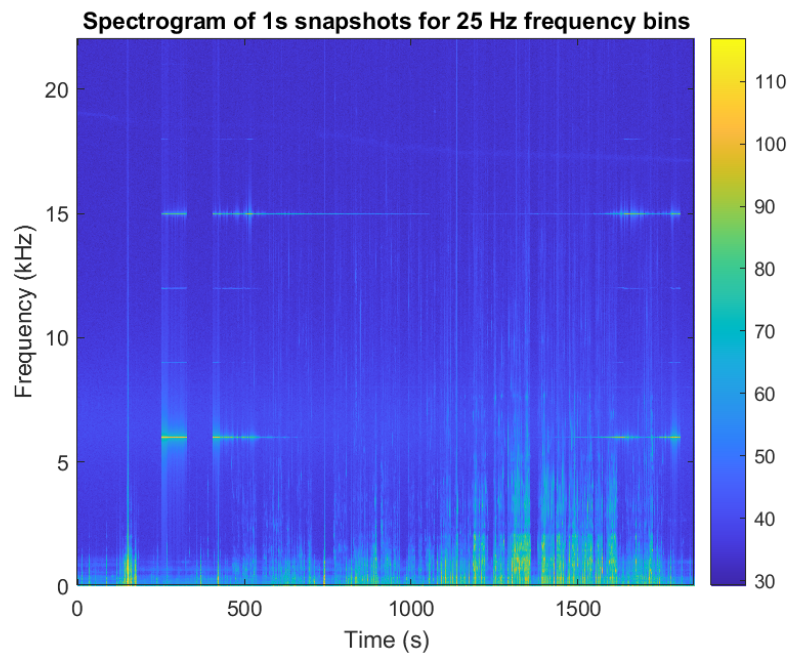
Figure 4-3b: Spectrogram b) shows a higher resolution plot via one second snapshots in time and 25 Hz frequency bins.
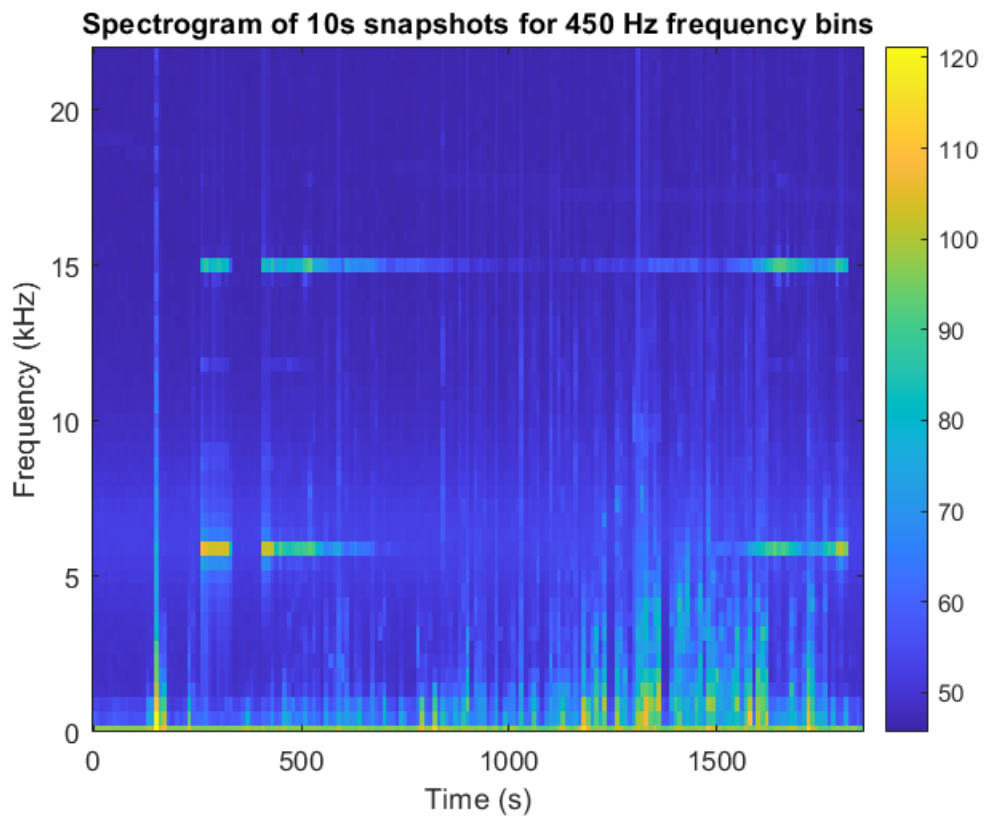
Figure 4-3c: Spectrogram c) uses ten second snapshots and 450 Hz frequency bins which more clearly identifies frequency bands with significant ambient noise and broadband interference.
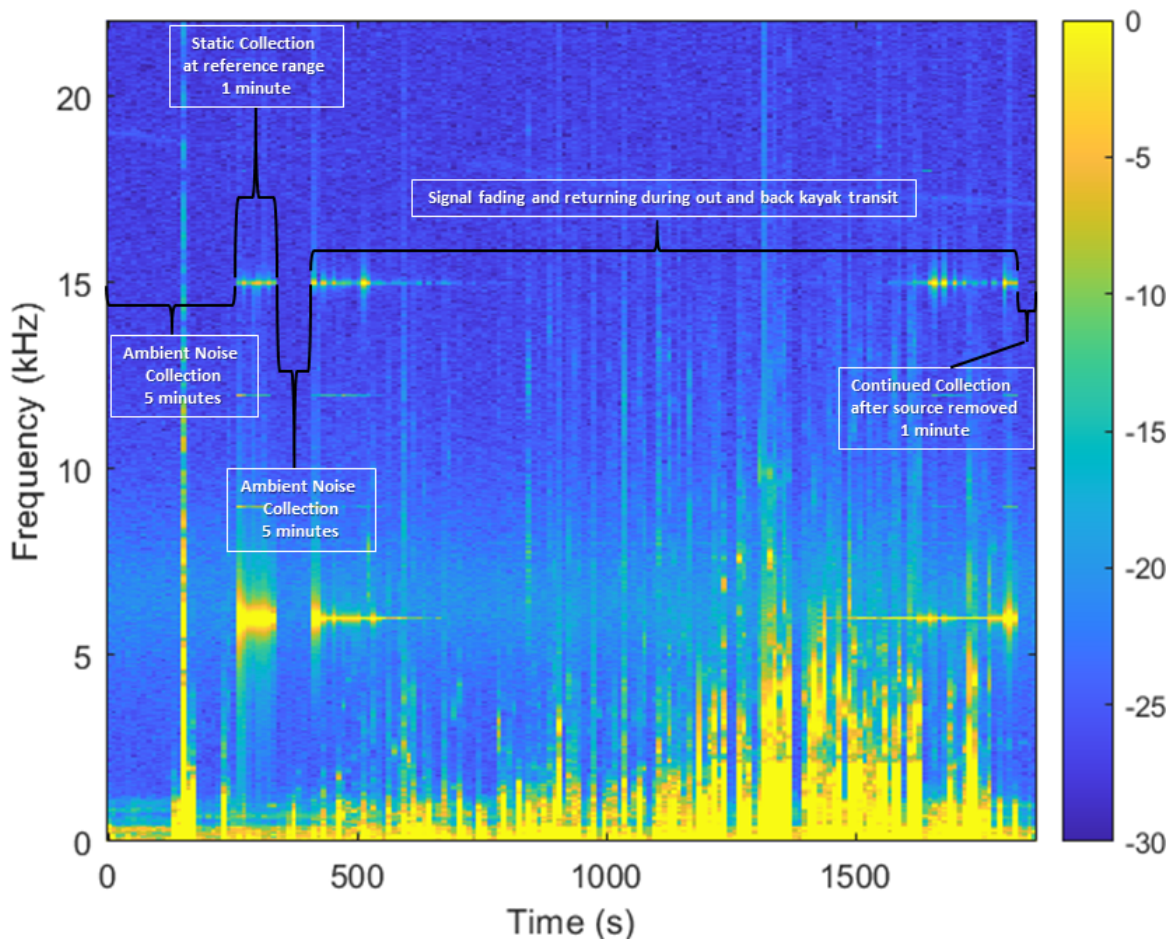
Figure 4-4: The spectrogram clearly depicts the sequence of events from Table 4.2 that occurred during the May 14, 2020 experiment through the energy content at each frequency bin. At a maximum range of 232 meters between source and receiver the signal visibly dissipates in the spectrogram.

Lubell LL-916C sound source at the selected frequency pairing.
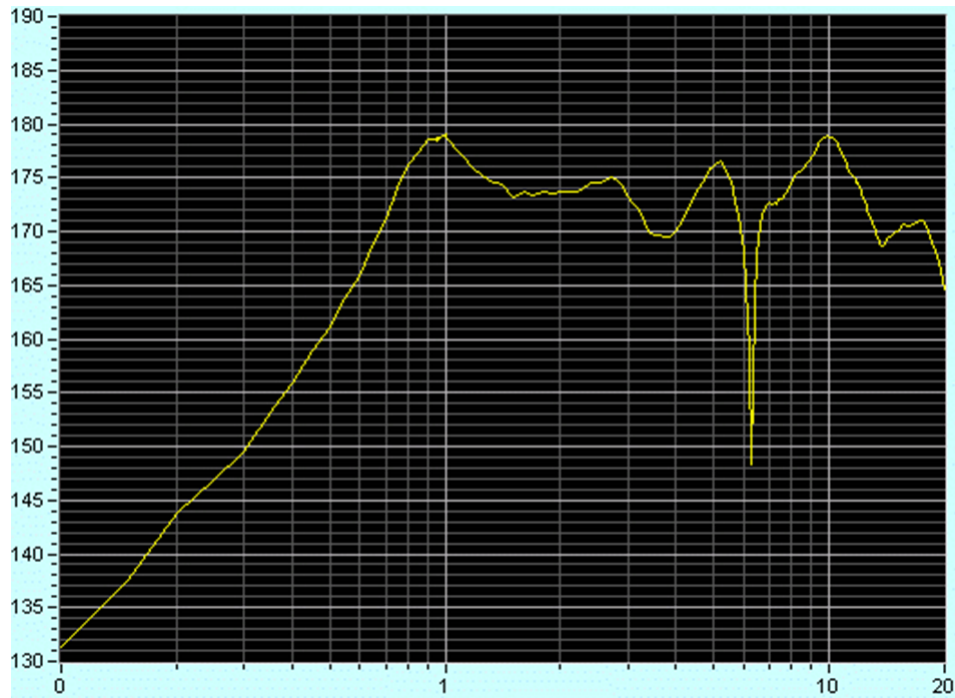
Figure 4-5: Sound Pressure Level (dB/μPa) versus Frequency (kHz) for Lubell
LL-916C [55]

A deep null appears in the sound pressure level plot for the source hardware shown in Figure 4-5. Lubell Labs website provides the frequency response in the source hardware documentation [55]. The frequency response could contribute to the large values for transmission loss at short ranges and the wide main lobe. The 6 kHz portion of this plot has a much steeper slope than the remainder of the curve and could impact the source's ability to maintain consistent output levels at this frequency. Chapter 5 provides an updated experimental protocol that factors in this frequency response should a similar source be employed again.

Given the shallow water environment and narrow operating channel, the continuous tones likely caused significant multipath within the environment, and particularly near the sound source location. Multipath effects raise RL at close ranges and complicates the data since the impacts decrease quickly as range increases. Near the source, multipath effects are almost immediate given the shallow environment, and one meter distance to surface and bottom boundary layers. The result is increased transmission losses in comparison to mathematical models. More importantly, these effects vary by frequency and may contribute

to some differences in the rate of increase for TL at each frequency.

Lastly, a lithium polymer battery was the power source for this experiment. Afterward, troubleshooting potential causes for the data recorded revealed that lead-acid batteries provided power to the source in previous experiments. This discrepancy occurred due to limited access to laboratory hardware. Based on feedback from technical experts at Lubell Labs, this is not ideal, and lead-acid batteries would be the preferred choice. The difference in power source is another potential cause for the rate of change in received sound level. Fluctuations at the source appear to be more impactful on the outbound leg, and may be mitigated by a more consistent power source.

4.2.3   Analyzing Received Signals

Now that the data is in time snapshots and frequency bins, the next step is to analyze the signal at the bands of interest, which correspond to the dual-tone continuous signal at 6 and 15 kHz. Throughout this analysis, varying snapshot lengths and bin widths show how averaging in frequency and time impacts the data. Since range estimation is the objective, the kayak's transit section in the time series is the focus of subsequent analysis. RL at 6 kHz and 15 kHz is denoted as RL_1 and RL_2 respectively.

The initial plan to calculate noise from time series sections when the source was not in the water did not adequately capture spatial and/or temporal variation of the ambient noise. The calculation measured ambient noise at the two source frequencies and spliced them into a single vector. The average of this vector sum gave the mean noise level while avoiding broadband spikes in the data.

Since the dual-frequency tone is continuous, the noise vector is instead sampled from a neighboring frequency band with adequate separation in frequency to avoid significant side-lobe contributions from either of the dual-tone frequencies. Altering this approach provides a better, if still not ideal, noise estimate. 9 kHz and 18 kHz represent noise estimates ($\tilde{N}$). The denoised signal is the measured received sound level minus the noise in dB at each frequency band.

$$RL - \tilde{N} = SL - TL$$

The first iteration averaged one-second snapshots in time with 25 Hz frequency bins, but

450 Hz frequency bins better approximated the extremely wide main lobes at the frequencies of interest. A moving mean function over the output shown in Figure 4-6 smooths the curves. This figure shows the measured received power at each frequency band of interest before and after smoothing. Then, it compares the two smoothed curves against each other.
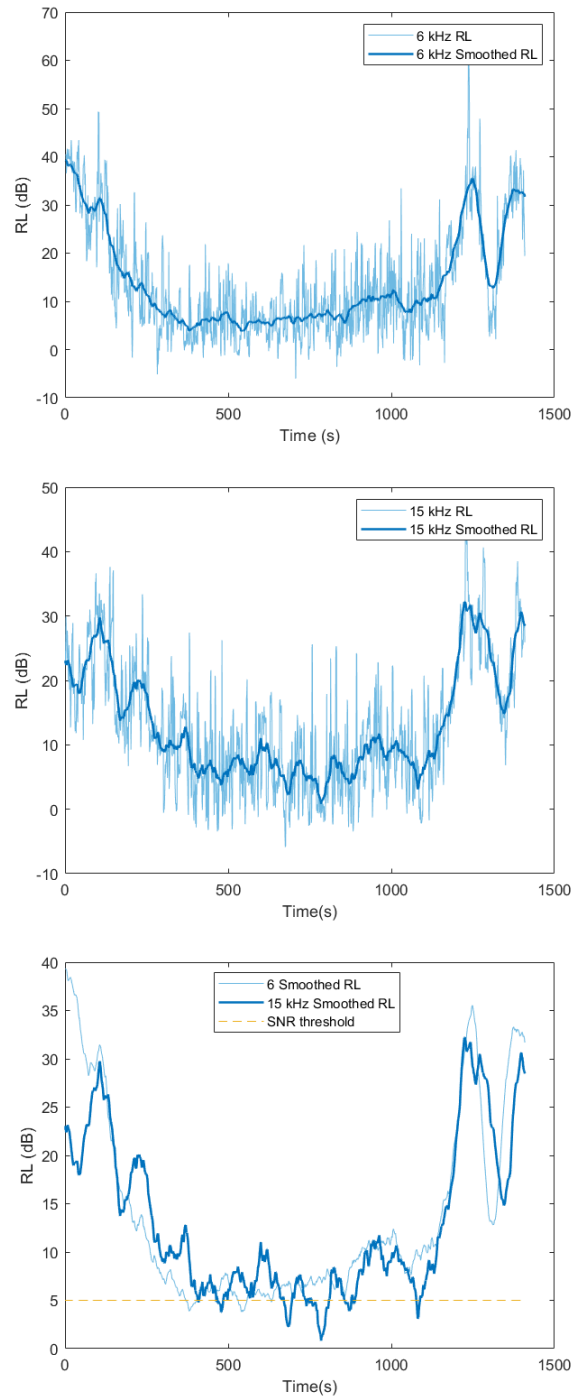
Figure 4-6: Received sound levels are compared in each frequency band.

Based on the received sound levels, there is a discrepancy between the two curves, particularly in the first half of the time series. The primary hypothesis is that the discrepancy is due to frequency-dependent multipath effects and potentially fluctuations at the source. Interestingly, the impacts are less apparent on the return route. There are two possible explanations for this phenomenon. It may be that the multipath in the environment from the continuous tone is steadily increasing at the beginning of the time series. This cause is feasible since the source was introduced to the water column and activated following a period of noise collection with no signal in the environment. However, such an increase would likely happen very quickly, and not be noticeable over the entire outbound transit. It is more likely that the pose of the kayak impacted these measurements. On the outward leg, the kayak backed away from the source before departing in the opposite direction, see Figure 4-7. However, when returning, the kayak was maneuvered in a manner that maintained the hydrophones facing the source. This change in pose could result in masking or variation of the multipath effect due to the kayak's position between the hydrophones and the source. Such an effect is magnified by the extremely shallow environment.
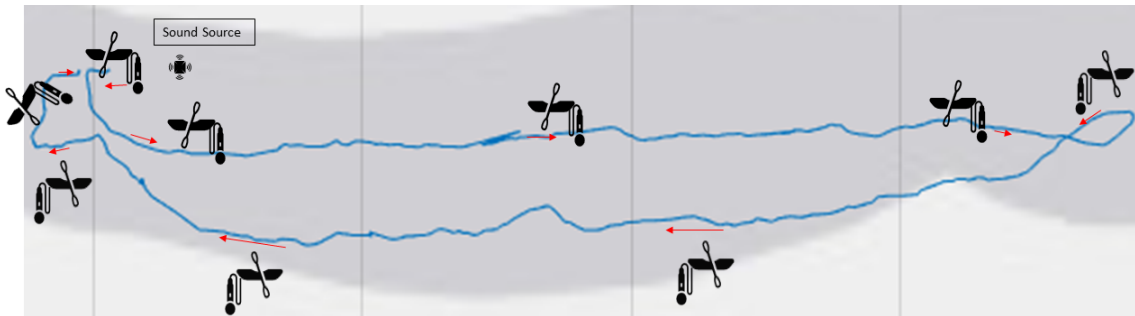
Figure 4-7: Representation of Kayak pose with respect to Sound Source, showing the hydrophone position relative to the source and the kayak body. The maximum distance between the source and receiver based on GPS is 232 meters.

After assessing the received sound level, the transmission loss at each frequency is the difference between the measured source level and the denoised received sound level. The average received level from the collection period at a one-meter reference distance provides an estimated SL. While this approach seemed logical in setup, there are concerns with the mirrored reflections and disparity in received sound level on the outbound leg of the transit. These disparities are assessed more closely by comparing the measured received sound level curves from the data with the mathematical model for geometric spreading and absorption, as well as Bellhop models run in MATLAB.
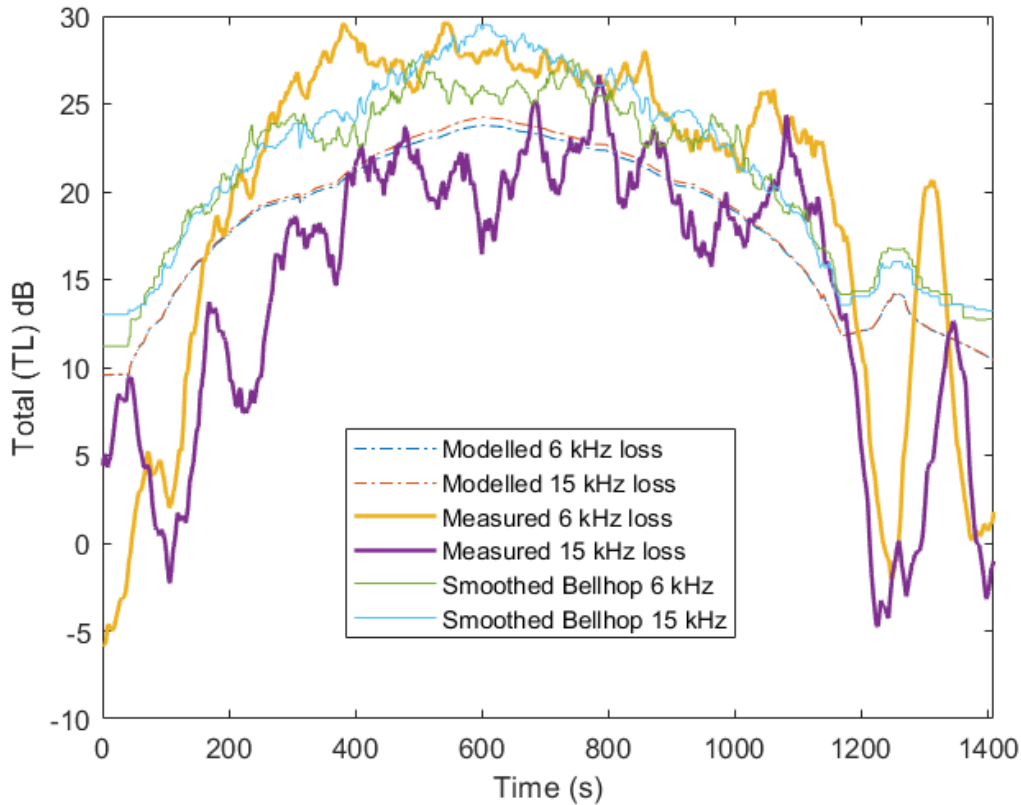
Figure 4-8: A comparison of mathematical models, Bellhop models, and measurement data for Environment 1 at 6 and 15 kHz. Bellhop accounts for frequency-dependent multipath effects that cause periods in which the lower frequency displays greater transmission loss. This factor supports the need for significantly increased frequency separation to avoid overlap that severely impacts estimation.

In Figure 4-8, there is a large difference in TL at frequencies of interest. Based on the close curves on the return transit, it appears that the 15 kHz tone has a slower rate of increase in TL on the outbound leg. This trend is counter to expectations that the higher frequency will always have increased transmission loss at increased ranges. Figure 4-9 compares these differences directly by plotting the measured TL against GPS derived ranges at each frequency.

4.2.4 GPS-derived Ranges

A Garmin inReach Explorer Plus provides the positions for a suitable ground truth to check the effectiveness of range estimation via absorption at differential frequencies. However, GPS data requires additional processing to match the acoustic data time series accurately.
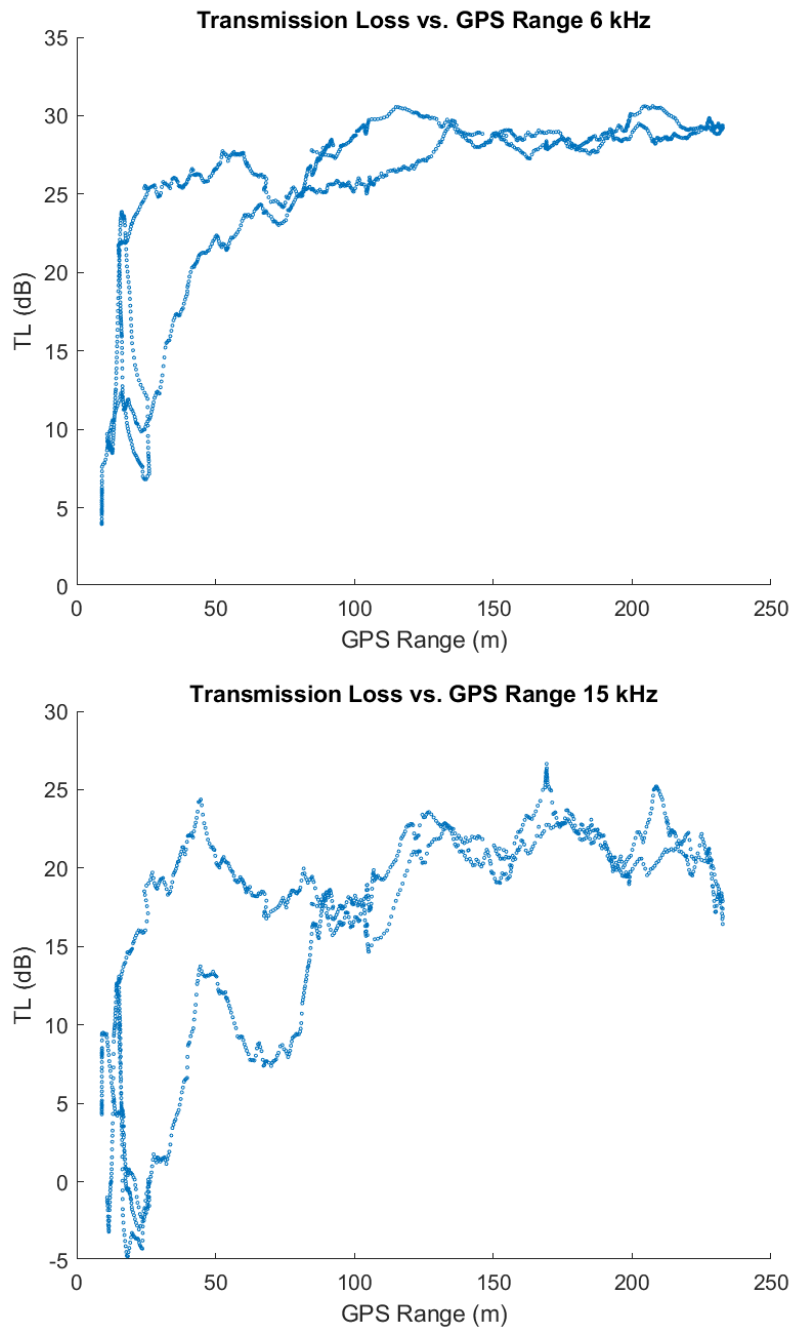
Figure 4-9: Transmission Loss vs. GPS Range for 6 kHz and 15 kHz respectively. This figure shows the disparity in transmission loss during outbound and inbound transits. The difference in transmission loss at the same ranges for 15 kHz is both greater and notable over a longer set of ranges. This is likely due to the frequency dependent effect of boundary loss on the signal at both short range and in very shallow water.

The device is designed to save battery life and will default to updating fixes at inconsistent time windows based on movement. GPS data also marks the source location during the experiment. Garmin maintains a web service that exports data files in various formats as well as desktop software. However, the desktop software provides more granular detail. Latitude, longitude, and time-stamps export as .gpx files and read into MATLAB.

Step 1: Latitude and Longitude convert to radians for the source location and the points along the transit.

$$(\text{degrees} * \pi)/180 = \text{radians}$$

Step 2: Next, the Haversine formula to calculates range from one coordinate point to another.

$$a = \sin^2(\Delta\phi/2) + \cos\phi_1 \cdot \cos\phi_2 \cdot \sin^2(\Delta\Lambda/2)$$

Where ϕ is latitude, Λ is longitude.

$$c = 2a \cdot \text{atan2}(\sqrt{a}, \sqrt{1-a})$$

and

$$r = R \cdot c$$

where atan2 is the two-argument arctangent representing the angle between the positive x-axis and a line to a non-zero point (x, y), $R = 6,371,000$ m is the mean radius for the earth, and the range is in meters. Figure 4-10 shows plots for the intermittently sampled data. The irregular sampling is noticeable in the x-axis with 341 samples over the 1,899 seconds of data. GPS fixes occur as frequently as every second, or as far apart as six minutes when not in motion.

The trimmed and time-stamped range vector focuses on the section recorded during the kayak transit. After trimming the excess data, interpolation matches it to the RL vectors in length. Figure 4-11 shows the time-stamped GPS data for comparison.

Based on Figures 4-8,4-9,4-7 and 4-11 the cause of the irregularities in the received sound level can be assessed further. This data reinforces the earlier assertion that irregularities in the received sound level could be related to the kayak's pose. Lower transmission losses
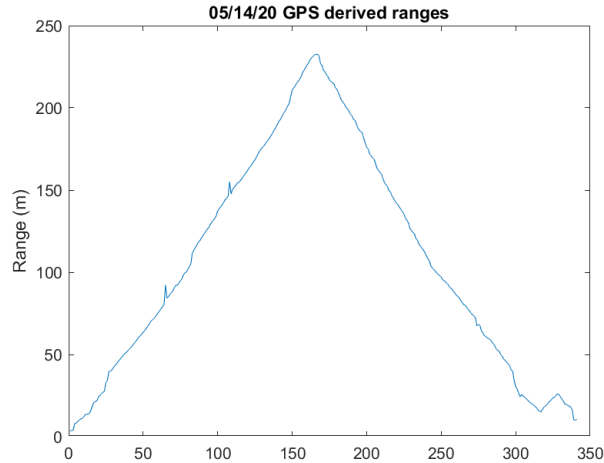
Figure 4-10: Irregularly sampled GPS-derived ranges
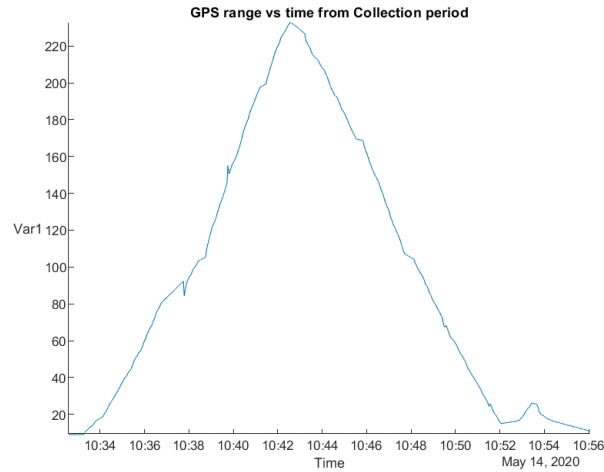
Figure 4-11: After processing GPS-derived ranges are useful for comparison to the estimate range during collection periods.

occur when the hydrophones have a clear path to the sound source, but the slope of the transmission loss is significantly increased on the outbound leg once the kayak is between the source and receiver. The indications on the return leg show this more clearly as the transmission loss drops drastically after 1200 seconds in the time series, but rebounds from zero to over 20 dB in transmission loss in less than 100 seconds. During this period, the kayak is near the source, but its position relative to the source and hydrophones is shifting, and then returns to the hydrophones directly facing the sound source. However, there is a slight peak represented by the Bellhop model, which may indicate that the setup is simply more sensitive due to the combination of surface and bottom losses than the models can

anticipate. The consistency of the curves with the models is promising, and better results may be feasible in a deep water environment with better options for frequency selection.

4.2.5 Thresholding for noise

A conservative signal-to-noise ratio of 5 dB for signal detection addresses concerns with the quality of the noise estimate. Figure 4-12 shows these sections in the received sound level plot.
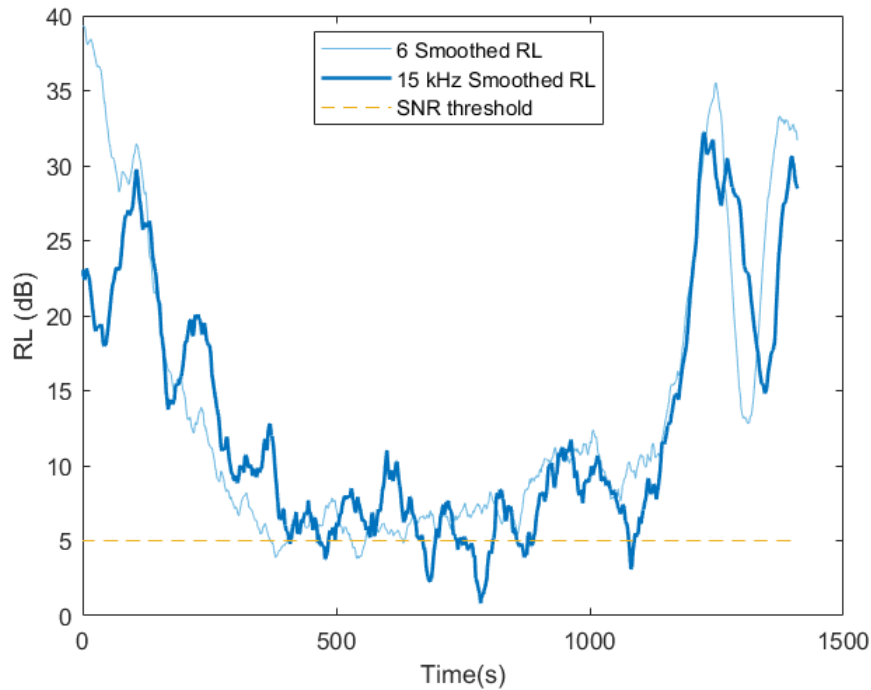
Figure 4-12: Received Sound Levels with cutoff for desired SNR

The conditions and data results from the experiment identify several issues with the source level detections. Therefore all range estimations are included, but figures highlight those made within 5 dB of the noise threshold for context. The noise estimate is removed, and therefore any detections below zero are viewed as detections based solely on noise. A 5 dB buffer zone identifies measurements that are close to noise.

Before making range estimations, an estimate for boundary loss is accounted for using BELLHOP. Since BELLHOP models transmission loss using geometric spreading loss, attenuation, and boundary loss, an estimate for boundary loss can be obtained by subtracting geometric spreading loss and Equation 3.19 for attenuation from BELLHOP's output for

transmission loss. This estimate is a minor adjustment, and can be improved with a better model of the environment, bathymetry and bottom layer. The boundary loss estimation for each frequency is then subtracted from their total transmission loss in order to focus the comparison on the difference in absorption.

The signals' lack of adequate separation becomes problematic in the range estimation. $\alpha_1 \approx 0.5$ dB/km and $\alpha_2 \approx 2.45$ dB/km are calculated based on the Francois-Garrison Equations and assumptions about the environment. These values give a separation of less than 2 dB/km, which is not ideal given the short ranges. The proximity of the frequencies is compounded by the shallow water environment, which heavily impacts the already sensitive difference in transmission loss. This impact is most evident when the transmission loss at 15 kHz is greater than at 6 kHz despite increasing range.

The range estimation in this environment is highly unreliable, though there is an improvement in the transit's return leg. The small difference in absorption rates between the two frequencies and the additional losses due to the frequency-dependent multipath in the shallow water environment led to estimations that consistently overestimate the range between one and two orders of magnitude from GPS-derived ranges.
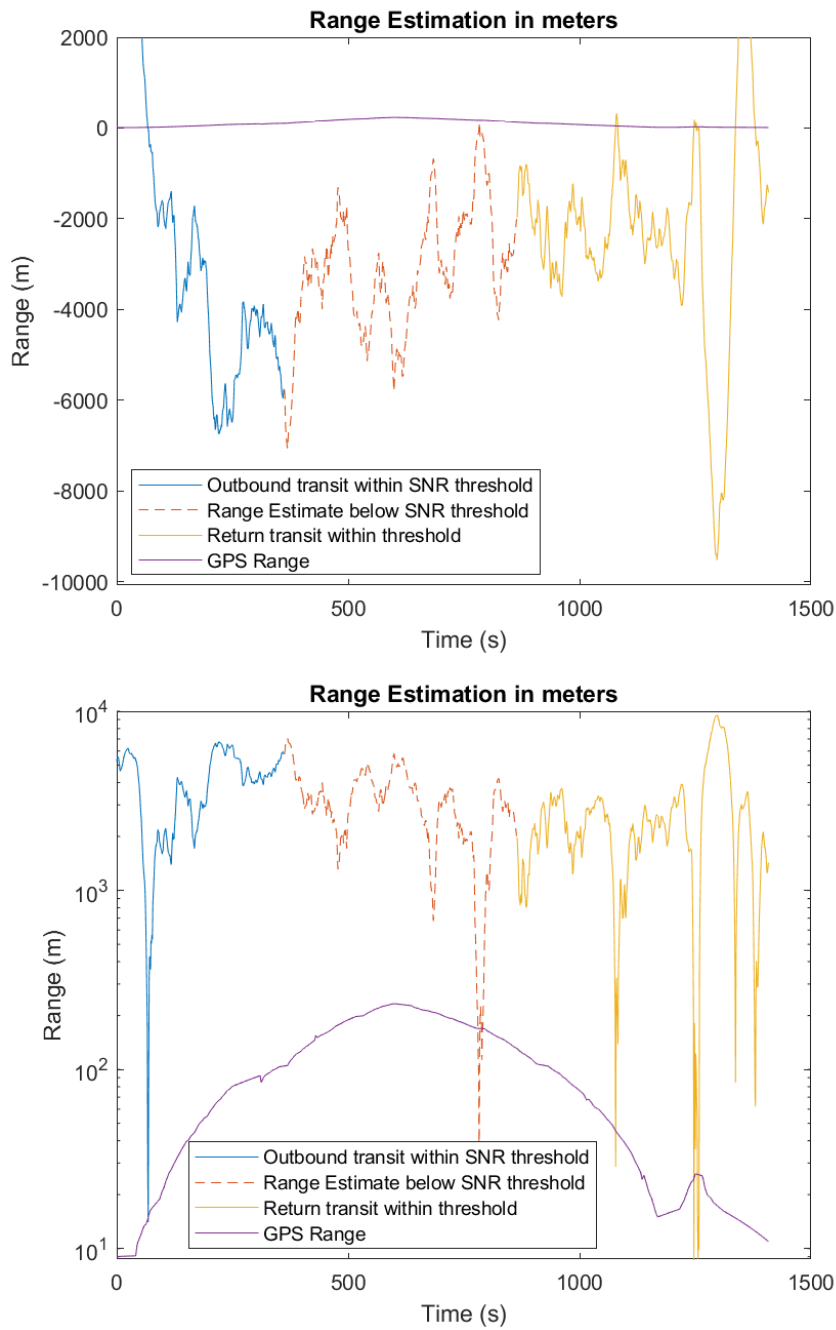
Figure 4-13: Range Estimation compared to GPS Ranges for 14MAY2020. The first plot shows a direct comparison with the estimate being several orders of magnitude away from ground truth. The second plot compares the two on a log-scale.

4.2.6 Adjusting the reference range

As discussed, the multipath effects and assumed source fluctuations are most significant at very short ranges, and early in the time series. In order to improve range estimate through SABRE the reference range can be reset to a further distance, thus avoiding the bulk of the effects. A distance of 23 meters is chosen heuristically based on the measured TL in Figure 4-8. The TL data at closer ranges is removed, and measurements at 23 meters are rest to zero making this range the new reference for transmission loss throughout the transit.

Transmission Loss for 6 and 15 kHz adjusted to 23 meter reference range
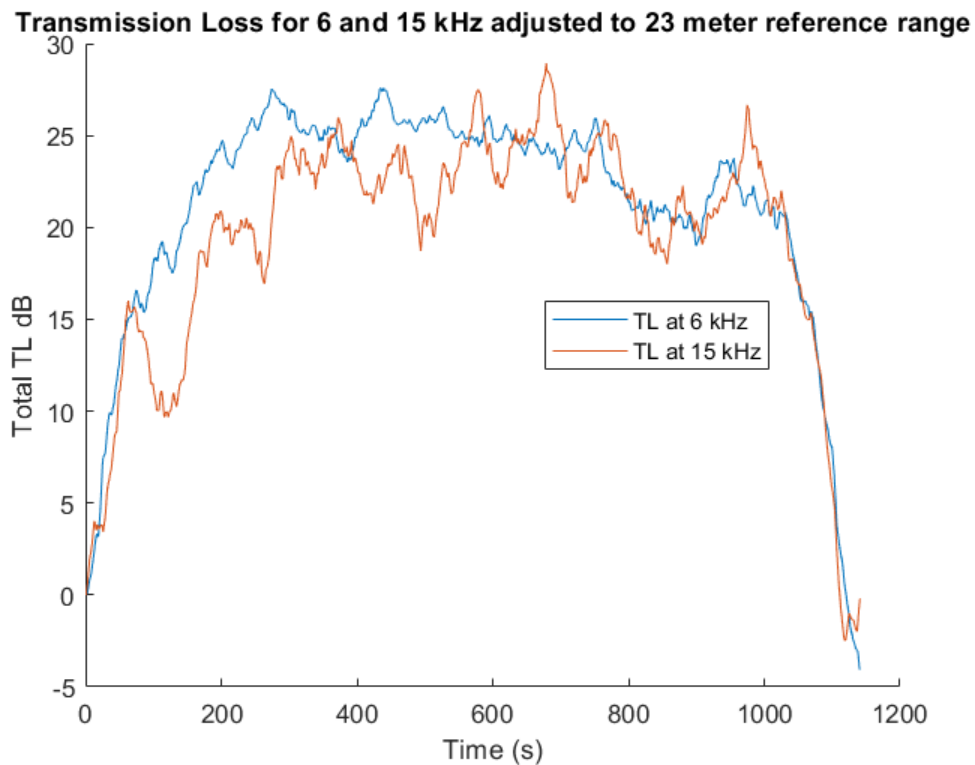
Figure 4-14: Transmission losses are compared after resetting the reference range for the source level. While there are still discrepancies in the outbound transit these curves align much more closely than when factoring in close range source level measurements.

The resulting curves are more closely aligned with expectations, but still display some inconsistencies during the outbound transit. Several potential causes for this have been identified, but the kayak pose seems to be the most consistent and easily confirmed contributor to the discrepancy.
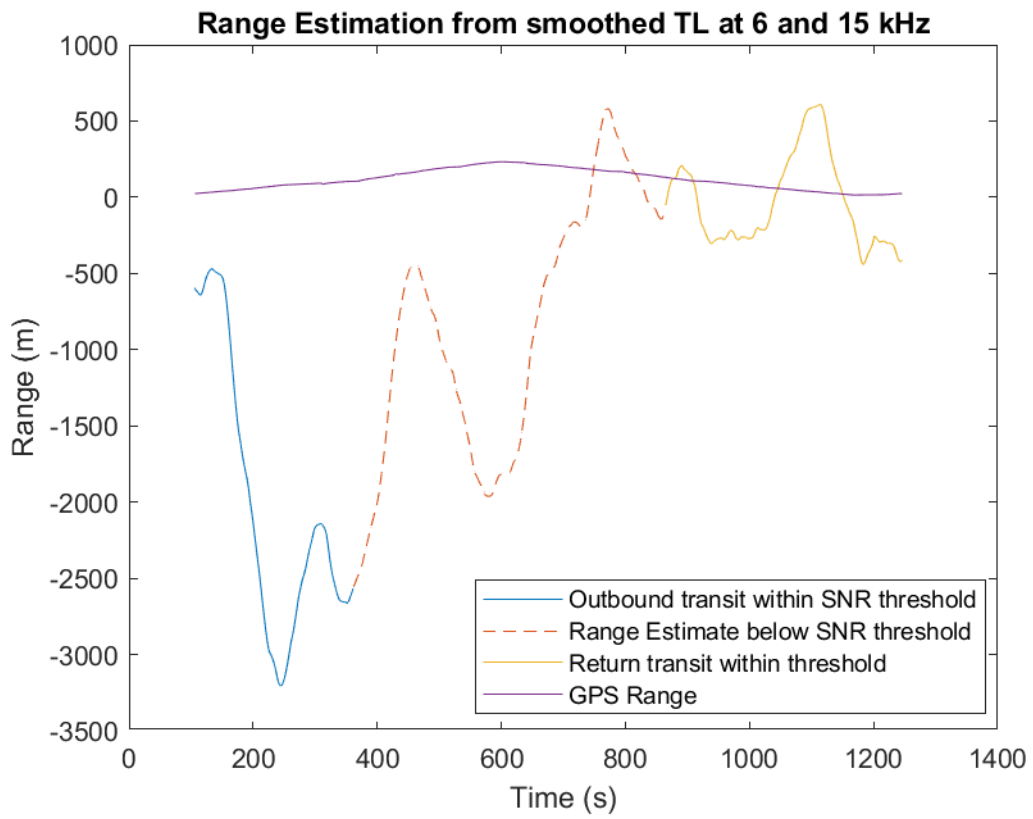
Figure 4-15: Updated range estimate based on new reference distance.
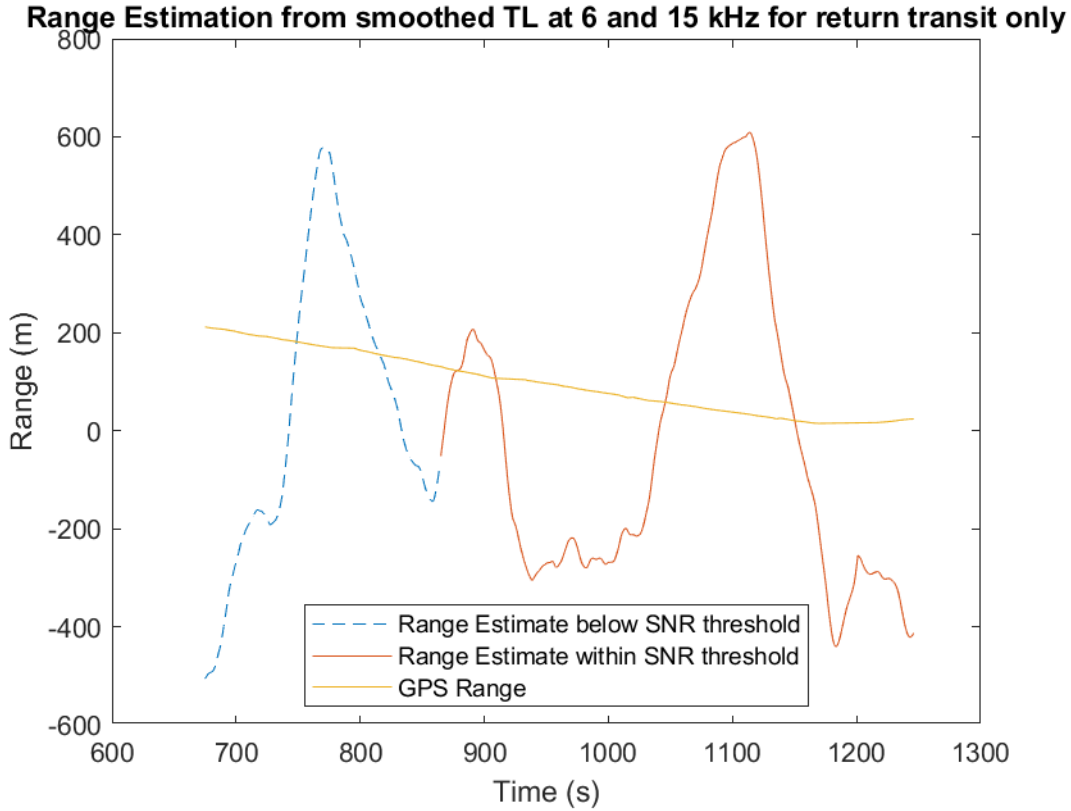
Figure 4-16: Range estimate focused on the return leg only.

Figure 4-15 shows a great improvement over the estimate for the full time series, but the inconsistencies in the outbound transit drastically increase error for that portion of the transit. The portion for which an estimate is feasible is further refined to focus on the return transit. During this period the kayak is not obstructing the path between the source and receiver which could explain the increased consistency in the measurements. This factor is much more significant given the extremely shallow conditions in the environment.

The most significant error on the return transit occurs well outside the 5 dB SNR threshold identified previously, but there is significant oscillation in the estimate. The error in range throughout the return transit is assessed in Figure 4-17. For the portion of the return transit that is within the desired SNR the mean error is 273.5 meters with a maximum error of 576 meters.
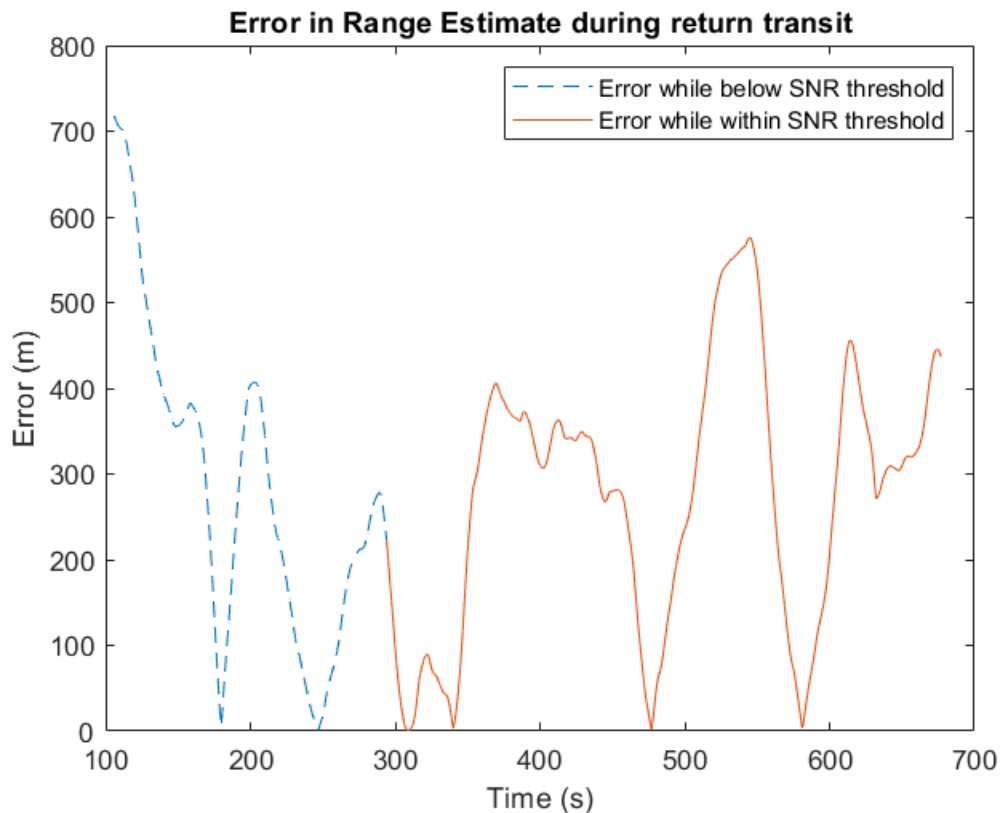
Figure 4-17: This figure shows the absolute value of the error between range estimates and GPS-derived ranges during the return transit. A mean error of 273.5 m and maximum error of 576 meters is achieved during this period. Given the worst-case scenario presented by this shallow water environment and limited frequency range of the source these results indicate a great deal of potential for SABRE as a viable low-cost technique.

4.2.7   Analysis of Results

Experimental data from May 14, 2020 revealed several limitations for SABRE in this extremely shallow environment. The pose of the vehicle became extremely impactful on RL given the small waveguide between the source and receiver, and the impacts from multipath made calculations more difficult. However, the environment and equipment utilized present a near worst-case scenario for range estimation. Even in this worst-case, there are elements in the data that show promise.

The choice of frequency was driven by the equipment available; however, a more in-depth analysis revealed many challenges implementing SABRE at such close frequencies. In 3-5, a log-linear trend shows that the models support such a comparison, but the outcome at these frequencies shows the low probability of success in Figure 4-18. The key to this plot is the oscillation of the difference in absorption between positive and negative values at close ranges. This difference is due to BELLHOP's inclusion of noise and multipath in the output and shows that these effects will negate estimation at close ranges. Estimation under these circumstances requires a more advanced statistical approach that deliberately models the multipath in a specific environment. To provide consistent estimations in its current form, SABRE relies on the empirical model's prediction that the higher of the two frequencies will have a greater rate of transmission loss that trends toward log-linear curve. In the second plot for Figure 4-18, this log-linear trend emerges at longer ranges, but it is not consistently positive until ranges greater than one kilometer. In an environment with depths averaging two meters or less, such as Bourne Pond, the multipath level likely precludes success, even at longer ranges.

The bottom composition in Bourne Pond is also of concern, especially given the small depths. Bourne Pond presents a muck bottom, which, despite its inclusion in modelling, likely requires more detailed bathymetry to model its impact on transmission loss accurately. This requirement is due to the bottom material's density gradually increasing with depth as opposed to a hard reflective boundary. A muck bottom instead acts as a medium of suspended scattering particles ending in a lossy bottom. Increased depth would lessen the impact of these factors by decreasing the number of interactions with the surface and bottom layers, but in this case, it has a profound effect on transmission loss that is not included in the models.

The most significant impact is the lack of depth in the environment, which drastically increases multipath, and magnifies the impacts from masking via the vehicle or other obstacles. At greater source and receiver depths, the effects from multipath and scattering caused by obstacles are mitigated due to fewer interactions with surface and bottom boundary layers and increased ray pathways between the source and receiver. The latter condition implies that there were be less impact from a change in vehicle pose than in shallow water. Figure 4-19 shows this difference through ray-trace plots in Environment 1 versus Environment 6, which show the difference in boundary interactions out to the first kilometer. These interactions significantly impact transmission loss and are more easily modelled in deep water environments.
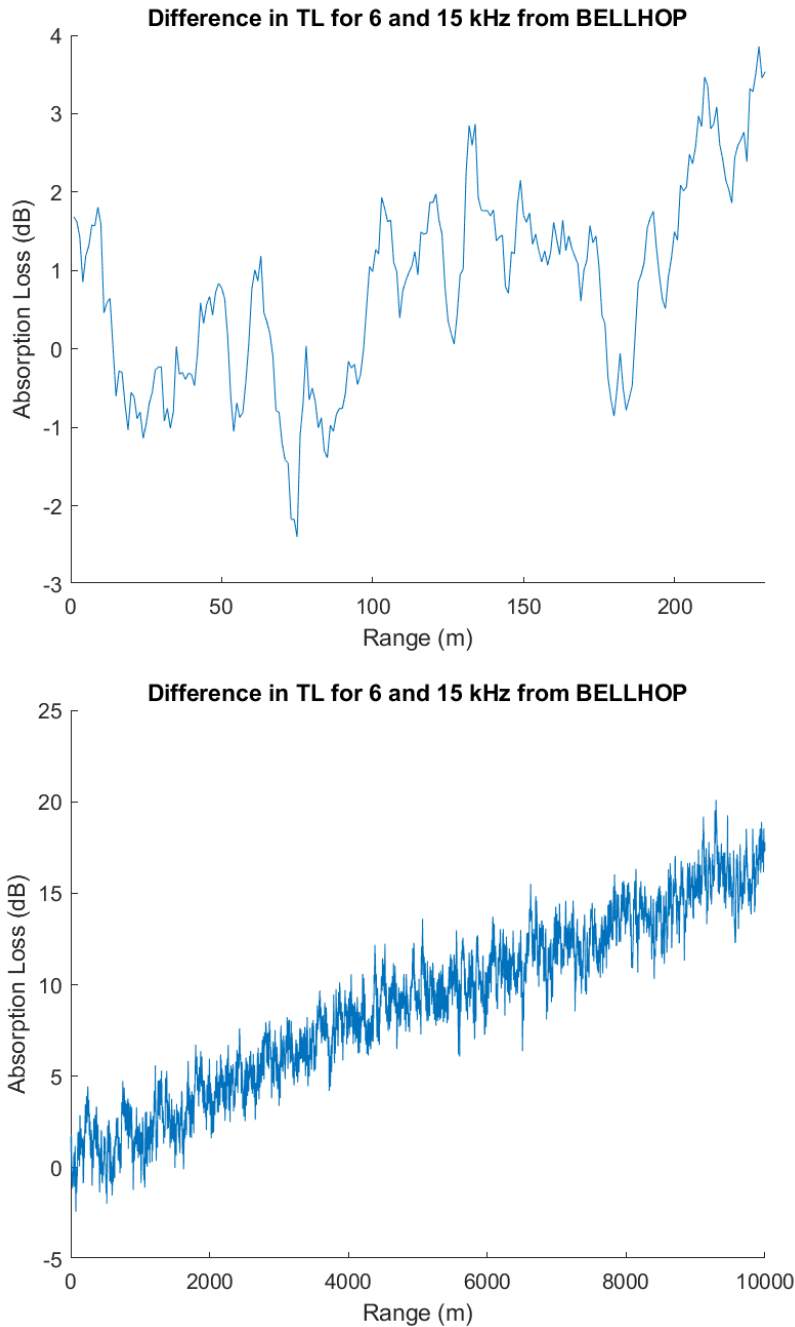
Figure 4-18: This figure shows a plot of the difference in transmission loss for 6 and 15 kHz at 230 meters in the first plot, and out to 10 kilometers in the second plot. The plots are meant to analyze the difference in transmission loss from BELLHOP models for the experimental environment on May 14, 2020 with a 2 meter depth. Since the range estimation is a function of the difference in transmission losses at two frequencies this difference provides insight into the likelihood that detection is feasible at certain ranges. This figure shows the extreme difficulty presented with a 6 and 15 kHz pairing at ranges less than 230 meters and the potential for improvement at longer ranges. However, the unpredictability, and high impact of multipath effects is also represented in the model which is a useful, but unreliable estimate.
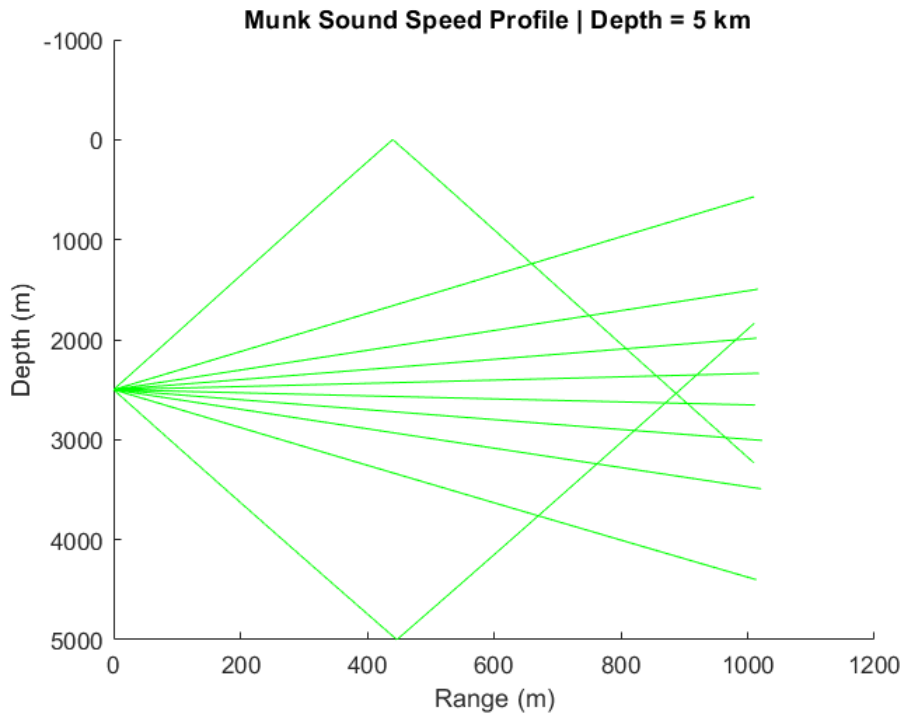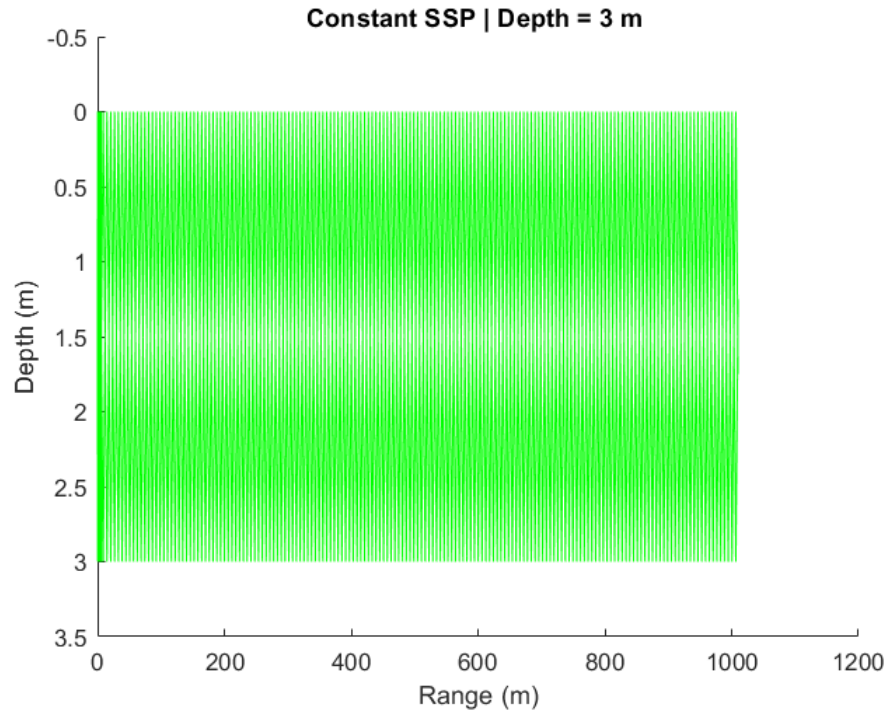
Figure 4-19: Ray plots from BELLHOP depict the ray paths for Environment 1 and 6. The ray paths are to be frequency independent, but the resulting loss from interaction with the surface and bottom boundary layers is frequency-dependent. Fewer rays are used in the Environment 1 Model, shown first, but the difference is clear, and the vastly increased number of interactions with the boundary layers significantly impacts the resulting transmission loss and the difficulty in modelling it.

Chapter 5

Conclusions and Future Work

5.1 Discussion

Marine environments present perhaps the most difficult challenges in the areas of communication and navigation. This environment is changes spatially and temporally with numerous environmental and equipment factors that impact results. This work has proposed a novel low-cost method, in SABRE, that estimates the differential transmission loss from a source broadcasting at multiple known frequencies to provide range estimations that do not require close time synchronization. Based on the theory and experimental results presented thus far, this chapter discusses the implications to AUV cost, localization accuracy, and opportunities for future work.

5.1.1 Cost

This work's primary objective is not to surpass the accuracy of existing undersea navigation approaches but to realize a scalable approach that allows vehicles to move in a formation undersea. To capture the difference in scalability, the Bluefin SandShark and Riptide AUVs serve as examples for the current standard [28] [29]. In [14], scalability is based on achieving a vehicle structure that is five percent of the minimum cost of existing low-cost systems, which translates to approximately $500. This requirement immediately negates the use of CSACs, large arrays, or low-frequency transducers.

The configuration for a custom analog front-end that meets frequency and amplitude accuracy requirements is detailed in [14]. Since SABRE requires only a low-cost MEMS

IMU, depth sensor, and single hydrophone onboard follower vehicles, the resulting platform size and cost meet the scalability requirements. It is also important to note that there is no limit placed on the number of vehicles within this communication structure as with acoustic modems. The comparative scalability assuming a fleet of current low-cost AUVs versus the approach proposed in this thesis rapidly favors an expensive leader with inexpensive followers. The leader is estimated to cost on the order of $50k. Initially, the $50k leader for the low-cost swarm makes it an expensive option, but the cost-per-vehicle lessens with each added vehicle. $50k is a conservative estimate for a vehicle with reliable navigation based on a higher-end INS and DVL, and intermittent or consistent access to the surface. This cost estimate is also valid for some feature-based approaches such as side-scan sonar, which could be used cooperatively in a multi-leader scenario, based on existing bathymetric maps, or identifying known landmarks for localization [30]. Based on these assumptions, at formations higher than six vehicles, methods that mitigate close time synchronization will become rapidly less expensive than current methods.

While this assessment is simplistic, it has important implications for the necessary accuracy and appropriate scenarios in which this swarming concept may be applicable. Assuming depth is maintainable via low-cost pressure sensors and that SABRE can estimate within a bounded error of 500 meters in deep water environments, lower cost swarms are achievable via this method with six or more vehicles covering areas on the order of square kilometers if all vehicles maintain the same depth. However, it is still feasible to utilize low-cost depth sensors in deep water to separate vehicles vertically but maintain equal distances from the lead vehicle. These factors are operationally dependent, but identify some flexibility in SABRE's employment for deepwater environments.

5.1.2 Accuracy

This technique does not compete with the accuracy of common techniques such as LBL and USBL which can estimate range within a meter on most systems. However, there are suitable low-cost techniques for comparison. The waveguide invariant techniques discussed in [45] are able to reduce position estimate error of 3 km from an INS down to 1 km. The potential for these techniques to be combined is discussed in the future work section of this chapter.

While LBL and USBL systems can reduce errors in range to the order of meters, their

associated limitations can be prohibitive to scalable swarms. SABRE can act as an aid to onboard INS by bounding the error associated with INS measurements. Given the environment and source limitations it is premature to draw strong conclusions about SABRE's accuracy, particularly in the deeper water environments for which it is intended. Additional experimentation in deep water environments is needed to demonstrate the extent to which SABRE can bound range errors for localization.

5.2   Conclusions

Given that the testing environment in this thesis was far from benign, it is too early to draw strong conclusions. This method will have decreased accuracy compared to cutting-edge navigation techniques but contributes to low-cost and scalability areas. SABRE is likely best suited as a means to bound error for a low-cost INS onboard follower vehicles in a swarm with a well-equipped leader or leaders. Such swarms may involve separations of hundreds of meters between vehicles. While this is the case, there is still an essential need for such a method when seeking significant spatial separation in the ocean to track changing measurements across space and time.

5.3   Future Work

5.3.1   Updated Experimental Protocol

Updated Experimental Protocol under Present Conditions

We can divide future work into immediate action items to update the experimental protocol for increased accuracy in SABRE's results and other avenues to approach improvement in the method.

First, even in the environment chosen and with less than ideal equipment, several adjustments can be made to improve the results. The first correction to the experimental protocol will be to move away from a continuous tone at two frequencies. Instead, a dual-frequency pulse of approximately 0.1 seconds every second will facilitate several improvements. A pulse per second signal will allow measurements for the signals of interest and the noise in the bands of interest at all points in the time series outside the pulses themselves. This minor change presents significant advantages in noise estimation and assesses the range limitation

for the source more accurately. This improvement will also require a less conservative SNR limitation for signal detection. This method can be further improved by using sets of equally spaced signals pulsed for 0.1 seconds every second. Post-processing, and eventually real-time estimation will be more flexible with sets of signals to choose from based on ambient noise levels, and variable ranges to the target as certain frequency pairings will perform better at short, mid, and long distance ranges.

The frequency selection itself can also improve. Subsequent experiments using a similar equipment setup should maximize frequency separation. Given feedback on inconsistencies above 18 kHz, 1 kHz and 17 kHz stand to improve detection levels' consistency. Figures 5-1 and 5-2 show the transmission loss curves at these two frequencies for the environment from May 14, 2020. In this case, it is unclear if the further frequency separation will provide any benefit. At close ranges, the greater wavelength at 1 kHz increases the impacts from multipath in shallow water, resulting in a significant initial loss at the lower frequency. However, the trend toward the 17 kHz signal surpassing the 1 kHz signal in transmission loss is more rapid than the previously chosen signals, and the absorption difference reaches a local maximum of 5 dB difference before reaching 1 km. The absorption difference for the 6 and 15 kHz pairing displays continued oscillation between -1 and 4 dB out to 1 km, as shown in Figure 4-18. These calculations utilize the same level of smoothing on both curves before comparing.

Estimating SL is difficult in almost any environment, but the impacts in very shallow water increase this challenge significantly. Two adjustments can facilitate an improved calculation for SL and separately the range estimate. An additional hydrophone should be set at a 1-meter reference distance from the source to provide a constant reference measurement for SL at every time step. This addition would not be intended as part of the final SABRE implementation, but is useful as a means to more accurately validate performance. While this will improve the confidence that the SL included in the measurement is not subject to fluctuation at the source, it will not overcome the suspected environmental impacts that lead to large RL values at close ranges and the subsequent spike in TL at longer ranges. However, a second step that will help mitigate this effect is establishing several reset ranges for calculation. Rather than a continuous out and back transit, deliberate stops at set ranges will allow for multiple samples and potentially better measurements. This technique should be combined with a higher amplitude signal for increased max range, and a longer overall
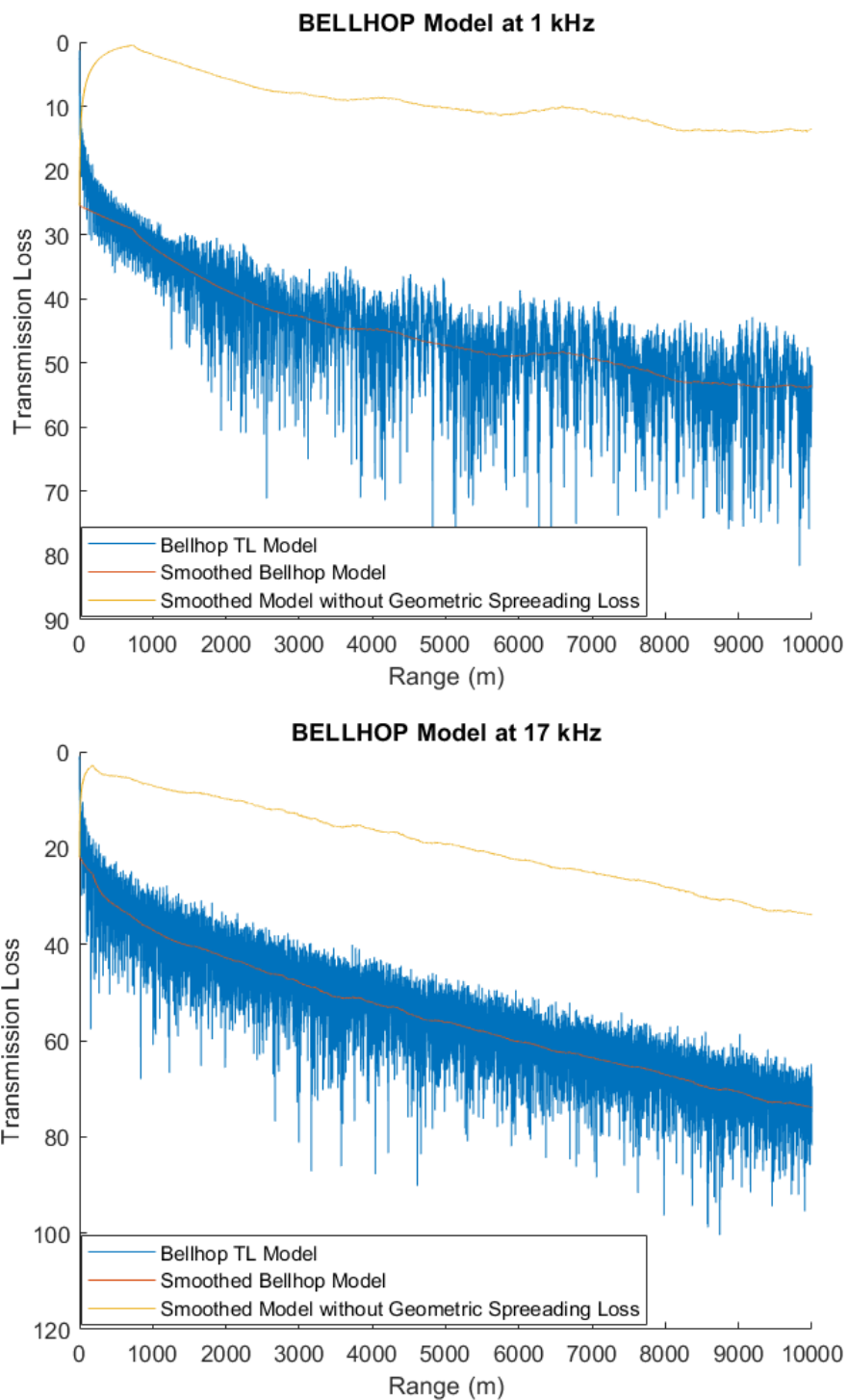
Figure 5-1: BELLHOP Models for 1 and 17 kHz show the greater difference in total transmission loss, and loss to absorption. Total transmission loss for each frequency is show as a raw and smoothed output from Bellhop with smoothing performed using a moving mean. Geometric spreading is then subtracted from the smoothed model to give insights into the contributions from absorption to the total transmission loss.
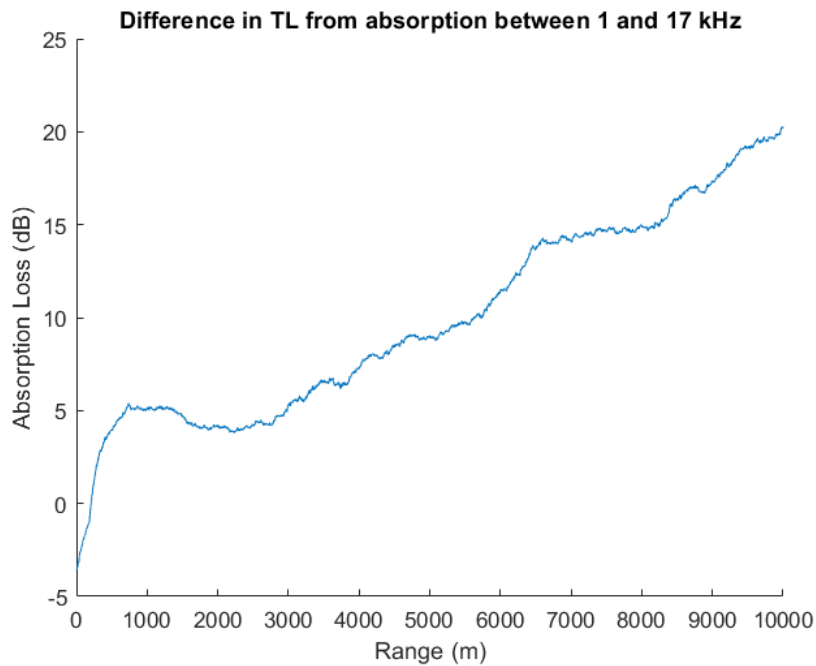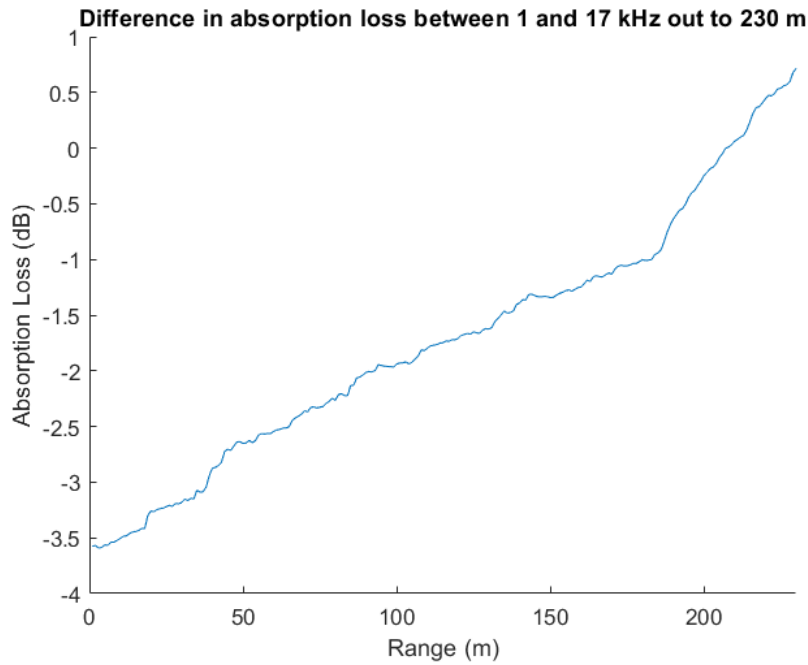
Figure 5-2: Models for prospective improvements in frequency pairing for the May 14, 2020 environment show that reliable range estimation will likely remain problematic at close ranges due to the initial transmission loss at longer wavelength lower frequencies. However, despite the drawbacks the increase in transmission loss difference at longer ranges may make reliable estimations feasible at distances greater than a kilometer with strong enough SL. These curves show the difference in absorption between the two frequencies at the range from May 14, 2020 experiment and out to 10 km.

transit.

Lastly, to more deliberately assess whether masking played a significant role in the large RL fluctuations in portions of the May 14, 2020 time series, subsequent experiments should be deliberate in establishing the position of the hydrophones relative to the sound source. Experiments should include trials where pose changes and trials where it remains the same throughout. During runs in which the pose is altered, these changes should be deliberately noted in the time series for the data to gauge the impact more closely.

Updated Experimental Protocol for Ideal Conditions

Despite methods to improve SABRE in the environment used for the May 14, 2020 experiment, it is apparent that the technique is better suited for deepwater environments at wider frequency separations. Still, future tests should address realistic use cases for underwater vehicle swarm formations. Therefore, Environment 4 serves as a vastly superior environment to the very shallow tidal pond from previous tests. Dual frequencies at 10 kHz and 40 kHz significantly improve frequency separation and, combined with the increased source and receiver depth, should produce superior results. Figure 5-4 shows the transmission loss and absorption curves for a 10 and 40 kHz pairing in Environment 4. Comparing 10 kHz and 40 kHz in this environment shows the improvement at close and longer ranges. The difference in transmission loss in the model stabilizes after only 50 meters in range. The variability from multipath becomes problematic after one kilometer, but it will require real-world data sets to determine the impact at that range. Regardless, according to models for both previous and prospective experiments, there appears to be vastly decreased sensitivity at 10 and 40 kHz in an environment that allows for increased depth.

5.3.2 Machine Learning

Machine learning is an algorithmic approach in which a predictive, classification, or other relevant model is designed to improve through additional data analysis. Models are built on the sample or training data in or to make predictions or decisions based on a probabilistic view derived from the training data. In this way, more data generally leads to a higher rate of success in machine learning.

Increasing use of machine learning for prediction and estimation algorithms presents significant opportunities for application in SABRE. SABRE presents several elements that
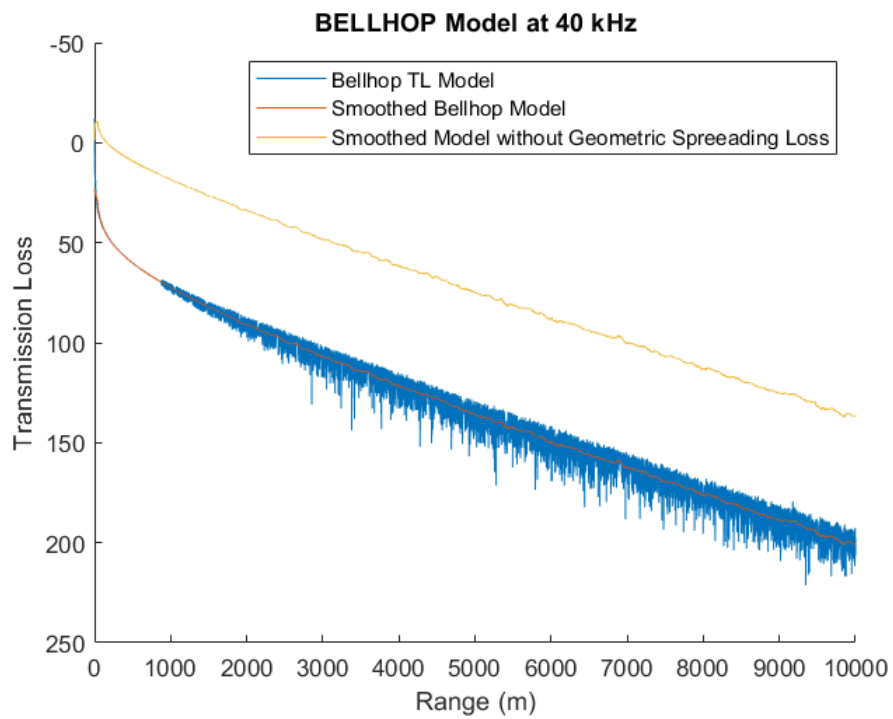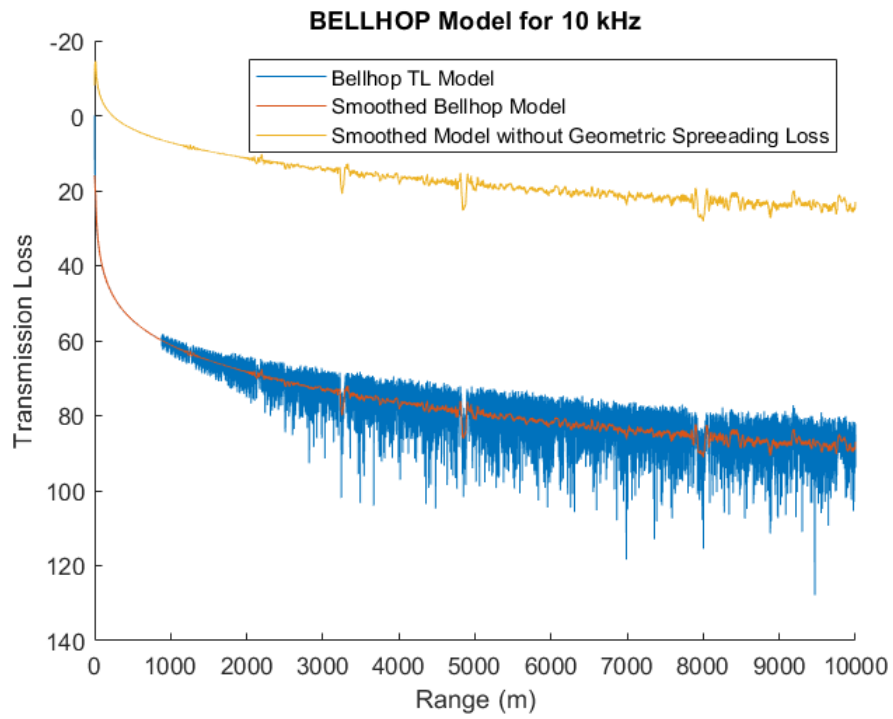
Figure 5-3: BELLHOP Models showing the total transmission loss and loss from Absorption at 10 and 40 kHz.
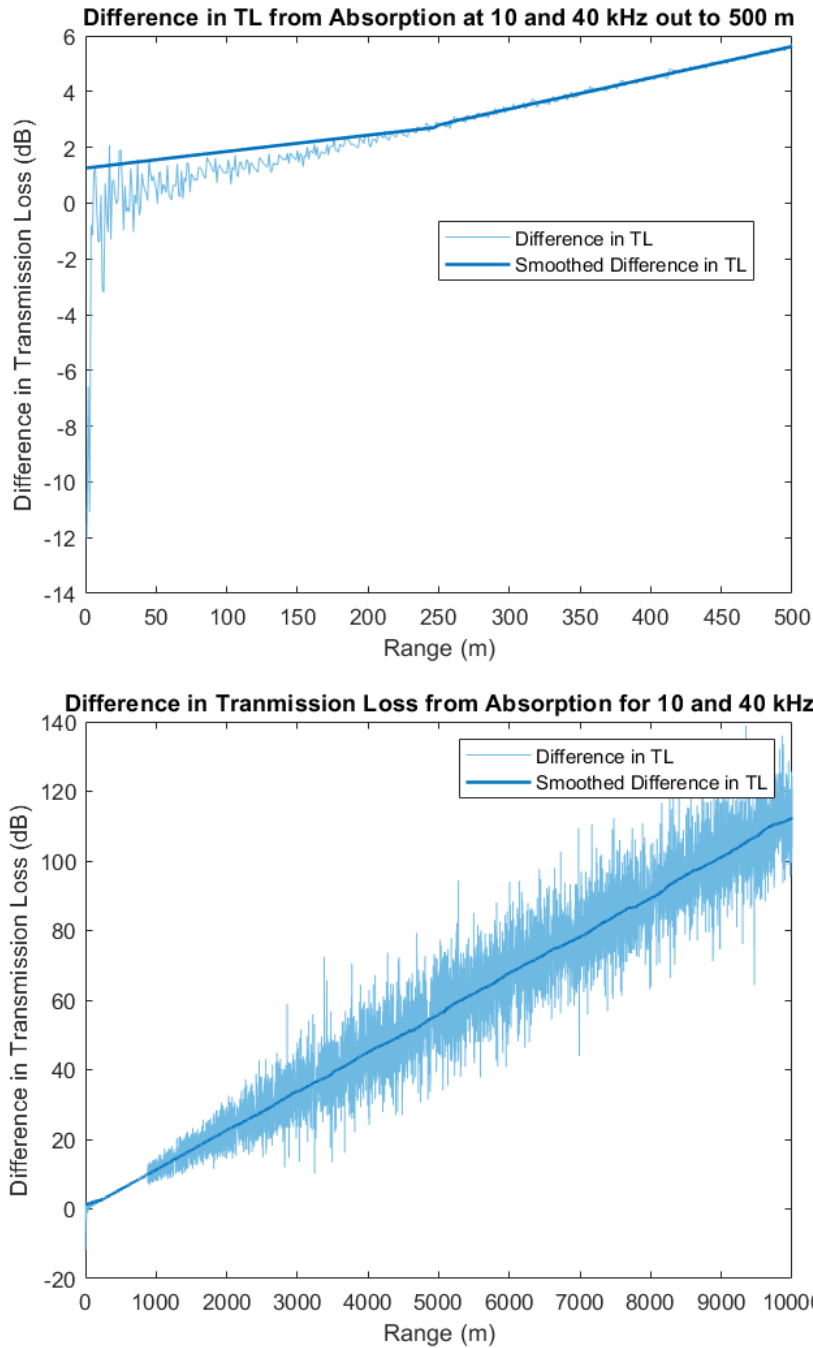
Figure 5-4: 10 and 40 kHz are analyzed as a prospective frequency pairing for Environment 4. Broader frequency separation and a deeper environment is significantly enhancing at shorter ranges as it leads to more rapid rates of increase in the differential transmission loss. Models indicate that significant multipath impacts to range estimation may occur at ranges greater than one kilometer, a significant improvement from shallow water tests. In the short range plot there is some variability in the model out to 200 meters before a stronger log-linear trend takes effect, and while this may make very close range estimates less accurate it is a vast improvement from closer frequencies whose separation oscillated from negative to positive out to ranges in the hundreds of meters.

The achievable accuracy from these frequencies must be assessed on data sets from real-world environments prior to making strong conclusions about their accuracy potential.

make machine learning a viable route, such as a base model from which measurements will vary, environmental parameters that can be set or inferred, and its structure as an optimization problem.

Machine learning is categorized into supervised and unsupervised learning. The critical difference is whether an initial classification structure is present or, as with unsupervised learning, the goal is to extract a description for patterns within input data without an initial class structure.

Similar to its use in speech and voice recognition, machine learning has been used for acoustic signal processing to support detection and classification, but in this case, the specific interest is in the acoustic environment and range estimation. The use of machine learning in conjunction with SABRE could mean a direct approach to range estimation based on pre-determined environmental parameters, or potentially an effort to extract the environmental parameters themselves to support range estimates. While other types of machine learning have been successfully applied in underwater acoustics, supervised learning through regression seems to be a logical approach for range estimation based on received sound level at a single hydrophone. Given the nonlinearity and stochasticity in ocean environments, this would best suit a multi-layered neural network or deep neural network. The multi-parameter dependencies between frequency and absorption favor this higher-complexity machine learning model that optimizes parameter weights in each layer of the neural network through back propagation [43] [42].

Machine learning techniques could work with SABRE to continuously build better predictive models for range prediction based on available data for a particular environment, and using GPS data for ground truth during training phases. One limitation may be the flexibility to multiple environments without retraining based on data specific to a new environment.

5.3.3   Matched Field Processing

Matched field processing (MFP) is a beamforming method that combines the physics of propagation with models for the spatial complexity of an acoustic field within an ocean waveguide. MFP was developed primarily to localize sound sources via range, bearing, and depth estimates, but can also be used to infer environmental parameters for modelling and navigation. MFP exploits the full acoustic field of the waveguide, and to do so, traditionally

utilizes a large aperture vertical array. At its foundation, MFP is a generalization of classical beamforming, but instead, it utilizes a steering vector derived from the Green's function of the medium [40]. MFP models the multipath structure's coherence to create a spatial matched filter that accounts for the entirety of the acoustic field.

While traditional methods have used wide-aperture multi-hydrophone arrays, recent work has explored narrow aperture arrays with reduced numbers of hydrophones [41]. This approach attempts to address limitations in MFP concerning environmental mismatching and the need for a significant aperture to sample the acoustic field adequately. Efforts have sought to work with the acoustic fields to create depth function matrices and normal mode amplitudes using smaller aperture arrays. Least squares are then applied to obtain estimates for remaining mode amplitudes, which inform calculations for the acoustic field and additional environmental parameters. While the least squares approach on a smaller aperture array has the significant benefit of reducing the necessary aperture, it remains sensitive to environmental mismatch.

In [39], a single hydrophone method that finds its foundation in MFP applies acoustic ray modelling, eigenray analysis, and the autocorrelation function to extract information from the environment for passive source localization. This approach models the transfer function from the source to the receiver for N eigenrays based on the multipath environment, similar to the approach with classical MFP. The acoustic ray modelling approach focuses on the arrival structure of the eigenray composed of its angle and the relative arrival delay of the eigenray (RADE). However, these aspects can be challenging to estimate, particularly in shallow water environments where the source signal is unknown. Based on the assumption that the signal is independent of the noise, [39] proposes an objective function for peak extraction passive source localization via the autocorrelation function of the received signal, a combination of autocorrelation functions for the source signal and the noise as well as the eigenray amplitudes. This approach is advantageous in environments that preclude RADE estimation and is of particular interest as a single hydrophone source localization technique.

There is potential to combine this method with range estimation via absorption, particularly in shallow water environments, to produce more accurate and more flexible results.

91

5.3.4 Waveguide Invariant

The waveguide invariant is discussed in Chapter 2 based on similar efforts to employ a single hydrophone and the waveguide invariant to estimate range and bearing to sources of opportunity [17]. While this work places emphasis on requirements for sources of opportunity, more recent work present in [45] by the same group indicates that such information could be gathered via alternate means, or the techniques could be applied in post-processing for source localization.

In Chapter 2, the waveguide invariant is described as the striations in the acoustic intensity pattern for broadband signals in a waveguide. Recent work such as [45] and [36] also focus on the usefulness of the β parameter as a means to derive other attributes from the environment, such as time-domain Green's functions or reference ranges between source and receiver.

While alone these techniques are an abundant field of research that shows promise for localization and characterization for the environment, there is potential for the mutually supporting information produced by SABRE and waveguide invariant techniques to create a mutually supporting algorithm that provides range estimate to support enhanced β prediction as well as a means to bound error in the absence of sources of opportunity through SABRE. SABRE and Doppler shift techniques for bearing could also substitute for the desired automatic identification system (AIS) data required for some waveguide invariant algorithms. This adjustment would limit the need for additional equipment on the AUV, such as acoustic modems, that would put limitations on swarms.

5.4 Summary

This thesis has proposed a novel method for range estimation using a single hydrophone that does not rely on close-time synchronization. The main contribution of this approach is to provide options for scalable low-cost swarms in an undersea environment.

Due to the extreme shallow water environment, several factors must be addressed in order to reliably validate, reproduce and improve upon the accuracy displayed for the return transit on the May 14, 2020 experiment. Experiments in deeper environments with wider frequency ranges must be tested. A key component to future tests should be to determine if the impact of vehicle pose is adequately mitigated in deeper water. To that end, this

chapter proposed two updated protocols to further assess the overall feasibility for SABRE in conjunction with scalable swarms. These protocols address improvements for estimation within a similar environment, which we identify as one of the most difficult. However, we also identify an improved environment for testing and assessment of SABRE's achievable accuracy.

This work successfully identified the theory, modelling techniques, and collection methods that will be used in future testing along with the previously stated lessons learned. While the results are not conducive to strong statements about SABRE's accuracy, the combination of BELLHOP modelling with existing theory and signal processing techniques provides the framework for further evaluation of technique in deepwater environments.

Lastly, each technique presented in the future work section of this chapter has its advantages and limitations, but advancements in localization will likely include combinations of range estimation algorithms that create flexibility to specific environments, and robustness to missing information. Machine learning in acoustic localization has had some success in using acoustics-based modelling to inform machine learning algorithms. This hybrid computational approach will lead to more robust and accurate solutions while preserving the approach's low-cost scalability. With further testing in deepwater environments, SABRE will continue to be evaluated as a tool in a continuum of solutions for underwater localization as part of the effort to support large scale underwater swarms at achievable costs thresholds.

Appendix A

List of Acronyms

AIS   automatic identification system

AUV   autonomous underwater vehicle

CSAC   chip-scale atomic clock

DAQ   digital acquisition

DVL   Doppler velocity log

EKF   extended Kalman filter

GPS   global positioning satellite

IMU   inertial mapping unit

INS   inertial navigation system

iUSBL   inverted ultra-short baseline

LBL   long baseline

MEMS   micro-electro-mechanical systems

MFP   matched field processing

MgSO4   magnesium sulfate

MIT   Massachussetts Institute of Technology

OWTT   one-way travel time

pH   potential of hydrogen

PSD   power spectral density

RADE   relative arrival delay of the eigenray

SABRE   signal absorption-based range estimator

SBL   short baseline

SLAM   simultaneous localization and mapping

SNR   signal-to-noise ratio

SOO   source of opportunity

SPHERES   Synchronized Position Hold Engage and Reorient Experimental Satellite

TDMA   time-division multiple access

TOF   time of flight

TWTT   two-way travel time

USBL   ultra-short baseline

WHOI   Woods Hole Oceanographic Institution

Bibliography

[1] Barnes, Christopher, et al. (2013) "Challenges, Benefits, and Opportunities in Installing and Operating Cabled Ocean Observatories: Perspectives From NEP-TUNE Canada" in IEEE Journal of Oceanic Engineering, vol. 38, pp. 144-157. doi: 10.1109/JOE.2012.2212751

[2] S. Chung, A. A. Paranjape, P. Dames, S. Shen, and V. Kumar. (2018) "A Survey on Aerial Swarm Robotics," in IEEE Trans. on Robotics, vol. 34, no. 4, pp. 837-855. doi: 10.1109/TRO.2018.2857475

[3] F. Irvin, J.C. Murray, S. Licheng; Z. Chun; S. Yue. (2014) "Development of an autonomous micro robot for swarm robotics," 2014 IEEE Int. Conf. on Mechatronics and Automation, vol., no., pp.635,640, 3-6 doi: 10.1109/ICMA.2014.6885771

[4] B. Lendon. "U.S. Navy could 'swarm' foes with robot boats." (2014, October 12) Retrieved July 17, 2020, from https://www.cnn.com/2014/10/06/tech/innovation/navy-swarm-boats/

[5] M. Saska, V. Vonasek, T. Krajnik, L. Preucil. (2012) "Coordination and Navigation of Heterogeneous UAVs-UGVs Teams Localized by a Hawk-Eye Approach." Proceedings of 2012 IEEE/RSJ Int. Conf. on Intelligent Robots and Syst. doi: 10.1109/IROS.2012.6385517.

[6] JC McWilliams. (2016) "Submesoscale currents in the ocean." Proc. R. Soc. A 472: 20160117. http://dx.doi.org/10.1098/rspa.2016.0117

[7] P. A. Miller, J. A. Farrell, Y. Zhao and V. Djapic. (2010) "Autonomous Underwater Vehicle Navigation," in IEEE Journal of Oceanic Engineering, vol. 35, no. 3, pp. 663-678. doi: 10.1109/JOE.2010.2052691.

[8] N. H. Kussat, C. D. Chadwell, and R. Zimmerman. (2005) "Absolute positioning of an autonomous underwater vehicle using GPS and acoustic measurements," in the IEEE Journal of Oceanic Engineering, vol. 30, no. 1, pp. 153-164. doi: 10.1109/JOE.2004.835249.

[9] Y. Watanabe, H. Ochi, and T. Shimura. (2012) "A study of inverse SSBL acoustic positioning with data transmission for multiple AUV navigation," 2012 Oceans - Yeosu, Yeosu, pp. 1-6, doi: 10.1109/OCEANS-Yeosu.2012.6263632.

[10] N. R. Rypkema, E. M. Fischell, and H. Schmidt. (2017) "One-Way Travel-Time Inverted Ultra-Short Baseline Localization for Low-Cost Autonomous Underwater Vehicles", IEEE Int. Conf. on Robotics and Automation (ICRA). doi: 10.1109/ICRA.2017.7989570.

[11] L. Paull, G. Huang, M. Seto, and J. J. Leonard. (2015) "Communication-constrained multi-AUV cooperative SLAM," 2015 IEEE International Conference on Robotics and Automation (ICRA), Seattle, WA,pp. 509-516, doi: 10.1109/ICRA.2015.7139227.

[12] E. Gallimore, J. Partan, I. Vaughn, S. Singh, J. Shusta, and L. Freitag. (2010) "The WHOI micro modem-2: A scalable system for acoustic communications and networking," OCEANS 2010 MTS/IEEE SEATTLE, Seattle, WA, pp. 1-7, doi: 10.1109/OCEANS.2010.5664354.

[13] Paull, L., Saeedi, S., Seto, M., Li, H. (2014) "AUV Navigation and Localization: A Review. IEEE Journal of Oceanic Engineering," 39(1), 131-149. doi:10.1109/joe.2013.2278891

[14] Fischell, E. M., Kroo, A. R., O'Neill, B. W. (2020) "Single-Hydrophone Low-Cost Underwater Vehicle Swarming. IEEE Robotics and Automation Letters," 5(2), 354-361. doi:10.1109/lra.2019.2958774

[15] Q. Liang et al. (2019) "Influences of temperature and salinity on holistic network performability of multi-AUV cooperative systems." ISA transactions. doi: 10.1016/j.isatra.2019.03.014

[16] N. Vedachalam, et al. (2019) "Autonomous underwater vehicles-challenging developments and technological maturity towards strategic swarm robotics systems." Marine Georesources Geotechnology 37.5: 525-538. doi: 10.1080/1064119X.2018.1453567

[17] A. Young, J. Soli, G. Hickman. (2017) "Self-Localization Technique for Unmanned Underwater Vehicles Using Sources of Opportunity and a Single Hydrophone," in OCEANS, pp. 1-6. doi: 10.1109/ACCESS.2017.2779835

[18] Francois, R. E., Garrison, G. R. (1982) "Sound absorption based on ocean measurements: Part I: Pure water and magnesium sulfate contributions," The Journal of the Acoustical Society of America, 72(3), 896-907. doi:10.1121/1.388170

[19] Francois, R. E., Garrison, G. R. (1982) "Sound absorption based on ocean measurements. Part II: Boric acid contribution and equation for total absorption," The Journal of the Acoustical Society of America, 72(6), 1879-1890. doi:10.1121/1.388673

[20] Jensen, F. B., Schmidt, H., Kuperman, W., Porter, M. (2011) "Computational Ocean Acoustics," New York, NY: Springer.

[21] R. J. Urick. (1983) "Principles of Underwater Sound," Peninsula Publishing. ISBN 9780932146625.

[22] H. F. Bezdek. (1973) "Pressure dependence of sound attenuation in the Pacific Ocean," JASA, vol. 53 (pg. 782-788) doi: 10.1121/1.1913392

[23] Porter, M., Duncan, A. (n.d.) "The Acoustics Toolbox," Retrieved June 23, 2020, from http://oalib.hlsresearch.com/AcousticsToolbox/

[24] Oppenheim, A. V., Schafer, R. W. (1999) "Discrete-time signal processing (2nd ed.)," Upper Saddle River, NJ: Prentice-Hall.

[25] A. T. Gardner and J. A. Collins. (2016) "A second look at Chip Scale Atomic Clocks for long term precision timing," OCEANS 2016 MTS/IEEE Monterey, Monterey, CA, pp. 1-9. doi: 10.1109/OCEANS.2016.7761268.

[26] M. Joordens, B. Champion. (2016) "Underwater Swarm Robotics: Challenges and Opportunities," Handbook of Research on Design, Control, and Modeling of Swarm Robotics. IGI Global, 2016. 718-740. doi:10.4018/978-1-4666-9572-6.ch026.

[27] E. M. Fischell, N. R. Rypkema, and H. Schmidt. (2019) "Relative Autonomy and Navigation for Command and Control of Low-Cost Autonomous Underwater Vehicles," IEEE RA-L, Vol. 4, Is. 2, pp 1800-1806. doi: 10.1109/LRA.2019.2896964.

[28] "Riptide family of autonomous undersea vehicles," (2020) Retrieved July 18, 2020, from https://www.baesystems.com/en-us/product/riptide-family-of-autonomous-undersea-vehicles

[29] "Bluefin SandShark AUV General Dynamics Mission Systems," (2020) Retrieved July 18, 2020, from https://gdmissionsystems.com/products/underwater-vehicles/bluefin-sandshark-autonomous-underwater-vehicle

[30] "JW Fishers SSS-100K Side Scan Sonar," (2015) Retrieved July 18, 2020, from http://www.jwfishers.com/products/sss.html

[31] Yoo, T. Kim, M. Yoon, S. Kim, D. (2020) "Performance Enhancement for Conventional Tightly Coupled INS/DVL Navigation System Using Regeneration of Partial DVL Measurements," Journal of Sensors, 2020, 1-15. doi:10.1155/2020/5324349

[32] Rudolph, D., Wilson, T. A. (2012) "Doppler Velocity Log theory and preliminary considerations for design and construction," 2012 Proceedings of IEEE Southeastcon. doi:10.1109/secon.2012.6196918

[33] S. D. Chuprov. (1982) "Interference structure of a sound field in a layered ocean," in Acoustics of the Ocean, edited by L. M. Breakhovskikh and I.B. Andreevoi, pp. 71–91. Nauka, Moscow.

[34] Cockrell, K. L. (2011) "Understanding and utilizing waveguide invariant range-frequency striations in ocean acoustic waveguides," doi:10.1575/1912/4328

[35] Khan, M. R., Das, B., Pati, B. B. (2020) "Channel estimation strategies for underwater acoustic (UWA) communication: An overview," Journal of the Franklin Institute, 357(11), 7229-7265. doi:10.1016/j.jfranklin.2020.04.002

[36] Song, H. C., Byun, G. (2020) "Extrapolating Green's functions using the waveguide invariant theory. The Journal of the Acoustical Society of America," 147(4), 2150-2158. doi:10.1121/10.0000969

[37] Cockrell, K. L., Schmidt, H. (2010) "Robust passive range estimation using the waveguide invariant," The Journal of the Acoustical Society of America, 127(5), 2780-2789. doi:10.1121/1.3337223

[38] Tesei, A., et al. (2015) "Passive acoustic surveillance of surface vessels using tridimensional array on an underwater glider," OCEANS 2015 - Genova. doi:10.1109/oceans-genova.2015.7271573

[39] Wang, H., Zhao, H. (2018) "Single Hydrophone Underwater Source Hyperbolic Passive Localization using Multipath Arrivals in Shallow Water," OCEANS 2018 MTS/IEEE Charleston. doi:10.1109/oceans.2018.8604304

[40] Baggeroer, A., Kuperman, W., Mikhalevsky, P. (1993) "An overview of matched field methods in ocean acoustics. IEEE Journal of Oceanic Engineering," 18(4), 401-424. doi:10.1109/48.262292

[41] Wang, Q., Wang, Y., Zhu, G. (2016) "Matched Field Processing Based on Least Squares with a Small Aperture Hydrophone Array. Sensors," 17(12), 71. doi:10.3390/s17010071

[42] Yang, H., Gao, L., Li, G. (2020) "Underwater Acoustic Signal Prediction Based on MVMD and Optimized Kernel Extreme Learning Machine," Complexity, 2020, 1-17. doi:10.1155/2020/6947059

[43] Yang, H., Lee, K., Choo, Y., Kim, K. (2020) "Underwater Acoustic Research Trends with Machine Learning: General Background," Journal of Ocean Engineering and Technology, 34(2), 147-154. doi:10.26748/ksoe.2020.015

[44] Yavasoglu, H., Tetik, Y., Gokce, K. (2019) "Implementation of machine learning based real time range estimation method without destination knowledge for BEVs," Energy, 172, 1179-1186. doi:10.1016/j.energy.2019.02.032

[45] Young, A. H., Harms, H. A., Hickman, G. W., Rogers, J. S., Krolik, J. L. (2020) "Waveguide-Invariant-Based Ranging and Receiver Localization Using Tonal Sources of Opportunity. IEEE Journal of Oceanic Engineering," 45(2), 631-644. doi:10.1109/joe.2018.2883855

[46] Dowling, A. P., Williams, J. E. (1989) "Sound and sources of sound," Chichester, England: E. Horwood.

[47] Moura, J. M., Lourtie, I. M. (1993) "Acoustic signal processing for ocean exploration," London, England: Kluwer Academic.

[48] Elmore, W. C., Heald, M. A. (1985). "Physics of waves," New York, NY: Dover.

[49] Frazer, L. N., Pecholcs, P. I. (1990) "Single-hydrophone localization. The Journal of the Acoustical Society of America," 88(2), 995-1002. doi:10.1121/1.399750

[50] Q. Yang, A. Lim, K. Casey, R.K. Neelisetti (2009) "An Enhanced CPA Algorithm for Real-Time Target Tracking in Wireless Sensor Networks. Int. J. of Distributed Sensor Networks", 619–643. doi: 10.1080/15501320802581318

[51] Chan, Y-T., and Frederick L. Jardine. (1990) "Target localization and tracking from Doppler-shift measurements", IEEE J. of Oceanic Eng (JOE). 15.3: 251-257. doi: 10.1109/48.107154

[52] L. Whitcomb, D. Yoerger, H. Singh. (1999) "Advances in Doppler-based navigation of underwater robotic vehicles", IEEE ICRA 1999, pp. 399-406 vol.1. doi: 10.1109/ROBOT.1999.770011

[53] H. L. Van Trees. (2002) "Detection, Estimation, and Modulation Theory, Optimum Array Processing (Part IV)", John Wiley & Sons, New York. pp. 51-52.

[54] X. Xiang, et al. (2010) "Coordinated Formation Control of Multiple Autonomous Underwater Vehicles for Pipeline Inspection. Int. J. of Advanced Robotic Systems", vol. 7, no. 1, pp. 75-84. doi: 10.5772/7242

[55] Lubell Labs (n.d.) "LL916C Pistonic Piezoelectric Underwater Speakers," Retrieved July 08, 2020, from http://www.lubell.com/LL916.html

[56] E. Fiorelli et al. (2006) "Multi-AUV Control and Adaptive Sampling in Monterey Bay," IEEE JOE, vol. 31, no. 4, pp. 935-948. doi: 10.1109/JOE.2006.880429

[57] J. Das, et al. (2011) "Towards Mixed-Initiative, Multi-Robot Field Experiments: Design, Deployment, and Lessons Learned," IEEE Int. Conf. on Intelligent Robots and Systems (IROS), pp. 3132-3139. doi: 10.1109/IROS.2011.6095068

[58] J. M. Soares, et al. (2013) "Joint ASV/AUV Range-Based Formation Control: Theory and Experimental Results", IEEE ICRA, pp. 5579-5585. doi: 10.1109/ICRA.2013.6631378

[59] J. M. Walls, et al. (2015) "Cooperative Localization by Factor Composition over a Faulty Low-Bandwidth Communication Channel", IEEE ICRA, pp. 401-408. doi: 10.1109/ICRA.2015.7139030

[60] C.R.German et al. (2012) "A long term vision for long-range ship-free deep ocean operations: persistent presence through coordination of Autonomous Surface Vehicles and Autonomous Underwater Vehicles." IEEE-AUV 2012 Conference. doi: 10.1109/AUV.2012.6380753

[61] N.E. Leonard et al. (2010) "Coordinated control of an underwater glider fleet in an adaptive ocean sampling field experiment in Monterey Bay." J. Field Robotics (JFR), 27: pp. 718-740. doi: 10.1002/rob.20366

[62] D. A. Paley, F. Zhang, and N. E. Leonard. (2008) "Cooperative Control for Ocean Sampling: The Glider Coordinated Control System." IEEE Trans. on Control Systems Tech., vol. 16, no. 4, pp. 735-744. doi: 10.1109/TCST.2007.912238

[63] T.C. O'Reilly, B. Kieft, M. Chaffey. (2015 May 18) "Communications relay and autonomous tracking applications for Wave Glider." IEEE OCEANS 2015-Genova (pp. 1-6). doi: 10.1109/OCEANS-Genova.2015.7271243

[64] M. Irving. (2018 April 09) "Aquabotix unleashes swarming, swimming, autonomous robots," New Atlas Marine.

[65] M. Johnson, L. Freitag, and M. Stojanovic. (1997) "Improved Doppler tracking and correction for underwater acoustic communications," 1997 IEEE Int. Conf. on Acoustics, Speech, and Signal Processing, Munich, pp. 575-578 vol.1. doi: 10.1109/ICASSP.1997.599703

[66] S. F. Mason et al. (2008) "Detection, synchronization, and Doppler scale estimation with multicarrier waveforms in underwater acoustic communication." IEEE Journal on selected areas in communications 26.9: 1638-1649.

[67] M. Stojanovic and J. Preisig. (2009) "Underwater acoustic communication channels: Propagation models and statistical characterization." IEEE communications magazine 47.1: 84-89.

[68] Bai, Chao, et al. (2019) "Digital underwater communication with chaos." Communications in Nonlinear Science and Numerical Simulation 73: 14-24. doi: 10.1016/j.cnsns.2019.01.027

[69] J. A. Knauss. (2005) "Introduction to Physical Oceanography." Waveland Press. ISBN 9781577664291.

[70] E. Gallimore et al. (2010) "The WHOI micromodem-2: A scalable system for acoustic modem communications and networking," MTS/IEEE OCEANS 2010, Seattle, WA,, pp. 1-7. doi: 10.1109/OCEANS.2010.5664354

[71] C. S. Clay, H. Medwin, (1977) "Acoustical Oceanography", New York Wiley pp. 544.

[72] F. De Rango, F. Veltri, and P. Fazio, (2012) "A multipath fading channel model for underwater shallow acoustic communications," 2012 IEEE International Conference on Communications (ICC), Ottawa, ON, pp. 3811-3815. doi: 10.1109/ICC.2012.6364590

[73] M.V. Jakuba, et al. (2015) "Feasibility of Low-Power One-Way Travel-Time Inverted Ultra-Short Baseline Navigation", IEEE OCEANS 2015, pp. 1-10.

[74] N. Kottege, and U. R. Zimmer. (2011) "Underwater acoustic localization for small submersibles," JFR, Special Issue: State of the Art in Maritime Autonomous Surface and Underwater Vehicles, Part 2, 28(1), pp. 40-69. doi: 10.1002/rob.20378

[75] USB-1608FS-Plus Series. (2019 September 27) Retrieved July 17, 2020, from https://www.mccdaq.com/usb-data-acquisition/USB-1608FS-Plus-Series